



UPPSALA
UNIVERSITET

*Digital Comprehensive Summaries of Uppsala Dissertations
from the Faculty of Science and Technology 408*

Hydrogen Storage Materials

*Design, Catalysis, Thermodynamics, Structure and
Optics*

CARLOS MOYSÉS GRAÇA ARAÚJO



ACTA
UNIVERSITATIS
UPSALIENSIS
UPPSALA
2008

ISSN 1651-6214
ISBN 978-91-554-7129-3
urn:nbn:se:uu:diva-8574

Dissertation presented at Uppsala University to be publicly examined in Högssalen, Ångströmlaboratoriet, SE-75121, Uppsala, Friday, April 11, 2008 at 10:15 for the degree of Doctor of Philosophy. The examination will be conducted in English.

Abstract

Graça Araújo, C M. 2008. Hydrogen Storage Materials. *Design, Catalysis, Thermodynamics, Structure and Optics*. Acta Universitatis Upsaliensis. *Digital Comprehensive Summaries of Uppsala Dissertations from the Faculty of Science and Technology* 408. x, 72 pp. Uppsala. ISBN 978-91-554-7129-3.

Hydrogen is abundant, uniformly distributed throughout the Earth's surface and its oxidation product (water) is environmentally benign. Owing to these features, it is considered as an ideal synthetic fuel for a new world energetic matrix (renewable, secure and environmentally friendly) that could allow a sustainable future development. However, for this prospect to become a reality, efficient ways to produce, transport and store hydrogen still need to be developed. In the present thesis, theoretical studies of a number of potential hydrogen storage materials have been performed using density functional theory. In NaAlH_4 doped with 3d transition metals (TM), the hypothesis of the formation of Ti-Al intermetallic alloy as the main catalytic mechanism for the hydrogen sorption reaction is supported. The gateway hypothesis for the catalysis mechanism in TM-doped MgH_2 is confirmed through the investigation of MgH_2 nano-clusters. Thermodynamics of Li-Mg-N-H systems are analyzed with good agreement between theory and experiments. Besides chemical hydrides, the metal-organic frameworks (MOFs) have also been investigated. Li-decorated MOF-5 is demonstrated to possess enhanced hydrogen gas uptake properties with a theoretically predicted storage capacity of 2 wt% at 300 K and low pressure.

The metal-hydrogen systems undergo many structural and electronic phase transitions induced by changes in pressure and/or temperature and/or H-concentration. It is important both from a fundamental and applied viewpoint to understand the underlying physics of these phenomena. Here, the pressure-induced structural phase transformations of NaBH_4 and ErH_3 were investigated. In the latter, an electronic transition is shown to accompany the structural modification. The electronic and optical properties of the low and high-pressure phases of crystalline MgH_2 were calculated. The temperature-induced order-disorder transition in Li_2NH is demonstrated to be triggered by Li sub-lattice melting. This result may contribute to a better understanding of the important solid-solid hydrogen storage reactions that involve this compound.

Keywords: Hydrogen-storage materials, Density functional theory, Molecular dynamics, Catalysis, Thermodynamics, Optics

Carlos Moysés Graça Araújo, Department of Physics and Materials Science, Ångströmlaboratoriet, Lägerhyddsv. 1, Box 530, Uppsala University, SE-75121 Uppsala, Sweden

© Carlos Moysés Graça Araújo 2008

ISSN 1651-6214

ISBN 978-91-554-7129-3

urn:nbn:se:uu:diva-8574 (<http://urn.kb.se/resolve?urn=urn:nbn:se:uu:diva-8574>)

To Emilene

Cover illustration:

An illustration of the hydrogen-storage in metal-organic framework-5 coated with Li atoms. O, C, Li and H atoms represented by red, black, blue and green balls. Zn atoms represented by the balls in the centre of the tetrahedra.

List of Papers

This thesis is based on the following papers, which are referred to in the text by their Roman numerals.

- I **Role of Catalysts in Dehydrogenation of MgH_2 Nanoclusters**
Peter Larsson, C. Moysés Araújo, J. Andreas Larsson, Puru Jena and Rajeew Ahuja
Proc. Natl. Acad. Sci. USA (PNAS) (Under revision).

- II **Role of titanium in hydrogen desorption in crystalline sodium alanate**
C. Moysés Araújo, R. Ahuja, J. M. Osorio Guillén and P. Jena
Appl. Phys. Lett. **86**, 251913 (2005).

- III **Dehydrogenation from 3d-metal doped NaAlH_4 : Prediction of catalysts**
A. Blomqvist, C. Moysés Araújo, P. Jena and R. Ahuja
Appl. Phys. Lett. **90**, 141904 (2007).

- IV **Ti-induced destabilization of NaBH_4 from first-principles theory**
C. Moysés Araújo, A. Blomqvist and R. Ahuja
J. Phys.: Condens. Matter **20**, 122202 (2008).

- V **Vacancy-mediated hydrogen desorption in NaAlH_4**
C. Moysés Araújo, S. Li, R. Ahuja and P. Jena
Phys. Rev. B **72**, 165101 (2005).

- VI **Electronic structure and hydrogen desorption in NaAlH_4**
S. Li, P. Jena, C. Moysés Araújo and R. Ahuja
Mater. Res. Soc. Symp. Proc. (MRS) **837**, N2.5.1 (2005).

- VII **On the structural and energetic properties of the hydrogen absorber $\text{Li}_2\text{Mg}(\text{NH})_2$**
C. Moysés Araújo, Ralph H. Scheicher, P. Jena and R. Ahuja
Appl. Phys. Lett. **91**, 091924 (2007).

- VIII **Thermodynamic analysis of hydrogen sorption reactions in Li-Mg-N-H systems**
C. Moysés Araújo, Ralph H. Scheicher and R. Ahuja

Appl. Phys. Lett. **92**, 021907 (2008).

- IX A comparative investigation of H₂ interaction in Cd- and Zn-based Metal Organic Framework-5**
P. Srepusharawoot, C. Moysés Araújo, A. Blomqvist, Ralph H. Scheicher and Rajeev Ahuja
In Manuscript.
- X Li-decorated metal-organic framework-5: A route to achieving a suitable hydrogen storage medium**
A. Blomqvist, C. Moysés Araújo, P. Srepusharawoot and Rajeev Ahuja
Proc. Natl. Acad. Sci. USA (PNAS) **104**, 20173 (2007).
- XI Pressure-induced structural phase transition in NaBH₄**
C. Moysés Araújo, R. Ahuja, A. V. Talyzin and B. Sundqvist
Phys. Rev. B **72**, 054125 (2005).
- XII Pressure-induced phase transition in ErH₃**
C. Moysés Araújo, A. Ferreira da Silva and R. Ahuja
Phys. Stat. Sol. (c) **241**, 3219 (2004).
- XIII Structural transition in lithium imide triggered by melting of cation sublattice**
C. Moysés Araújo, A. Blomqvist, Ralph H. Scheicher, and R. Ahuja
Submitted to Phys. Rev. Lett.
- XIV Electronic and optical properties of pressure induced phases of MgH₂**
C. Moysés Araújo and R. Ahuja
J. Alloys and Compd. **404-406**, 220 (2005).
- XV Electronic and optical properties of α , γ and β phases of MgH₂: a first-principle GW investigation**
C. Moysés Araújo, S. Lebègue, O. Eriksson, B. Arnaud, M. Alouani and R. Ahuja
J. Appl. Phys. **98**, 096106 (2005).
- XVI Quasiparticle and optical properties of BeH₂**
S. Lebègue, C. Moysés Araújo, O. Eriksson, B. Arnaud, M. Alouani and R. Ahuja
J. Phys.: Condens. Matter **19**, 036223 (2007).

Reprints were made with permission from the publishers.

The following papers are co-authored by me but are not included in this Thesis.

- **Structurally induced insulator-metal transition in solid oxygen: A quasiparticle investigation**
Duck Young Kim, S. Lebègue, C. Moysés Araújo, B. Arnaud, M. Alouani and Rajeev Ahuja
Phys. Rev. B (In press).
- **Spin-dependent conductance in nonmagnetic InGaAs asymmetric double barrier device**
C. Moysés Araújo, A. Ferreira da Silva, C. Persson, R. Ahuja and E. A. de Andrada e Silva
Brazilian Journal of Physics **34**, 632 (2004).
- **Electronic and optical properties of rutile titanium dioxide**
A. Ferreira da Silva, I. Pepe, C. S. Silva Brasil, Denis G. F. David, E. F. da Silva Jr., C. Persson, T. Lindgren, J. S. de Almeida, C. Moysés Araújo, and R. Ahuja
Phys. Stat. Sol. (c) **1**, S241 (2004).
- **Optical Properties of Oxide Compounds PbO, SnO₂ and TiO₂**
A. Ferreira da Silva, I. Pepe, C. Persson, J. S. de Almeida, C. Moysés Araújo, R. Ahuja, B. Johansson, C. Y. An and J.-H. Guo
Physica Scripta **T109**, 180 (2004).

Comments on my contributions

The research phases of the works developed in the present thesis for which I have partially contributed are illustrated by the marks in the table bellow. For those papers where I am the first author I have taken the main responsibility in performing the calculations, analyzing the data and writing the papers.

Papers	designing research	performing calculations	analyzing data	writing the paper
I	x	x	x	x
II	x	x	x	x
III	x		x	x
IV	x	x	x	x
V	x	x	x	x
VI		x	x	
VII	x	x	x	x
VIII	x	x	x	x
IX	x		x	
X	x	x	x	x
XI	x	x	x	x
XII	x	x	x	x
XIII	x	x	x	x
XIV	x	x	x	x
XV	x	x	x	x
XVI			x	

Contents

1	Introduction	1
2	Theoretical background	3
2.1	Density Functional theory	3
2.1.1	The many-body problem	3
2.1.2	The Hohenberg-Kohn theorems	4
2.1.3	The Kohn-Sham ansatz	5
2.1.4	Exchange-correlation functional approximations	7
2.2	Computational methods	7
2.2.1	The secular equation	7
2.2.2	The Bloch electrons and plane wave basis set	8
2.2.3	LAPW method	9
2.2.4	PAW method	11
2.2.5	Localized basis set	13
2.3	Force theorem and geometry optimization	14
2.4	Molecular dynamics	15
3	Hydrogen storage I: Chemisorption	19
3.1	Chemical hydrides classification	19
3.2	Hydrogenation mechanism	19
3.3	Thermodynamics	21
3.4	Role of catalysts on dehydrogenation	23
3.4.1	MgH ₂ nanocluster	23
3.4.2	Sodium alanate	25
3.4.3	Sodium borate	30
3.4.4	Vacancy mediated hydrogen desorption	32
3.5	Mixtures as a new strategy	33
4	Hydrogen storage II: Physisorption	37
4.1	Introduction	37
4.2	H ₂ adsorption in metal-organic frameworks	39
4.3	Functionalized metal-organic frameworks	42
5	Structural phase transition	45
5.1	Pressure-induced structural transformation	45
5.1.1	Thermodynamics	45
5.1.2	NaBH ₄	46
5.1.3	ErH ₃	47
5.2	Temperature-induced structural phase transition in lithium imide	49
6	Optical properties of saline hydrides	53
6.1	Complex dielectric function	53

6.2	GW quasi-particle	54
6.3	MgH ₂	55
6.4	BeH ₂	57
7	Conclusions and outlook	59
8	Sammanfattning	63
	Bibliography	67

1. Introduction

Hydrogen is one of the most abundant elements on earth and is able of releasing energy through chemical reactions with O_2 in heat engines and fuel cells producing only water as byproduct [1]. Owing to these features, it is being considered as a promising alternative to replace the harmful fossil fuels, which may not meet the worldwide demand for sustainable energy in the near future. However, hydrogen is not found in nature forming a pure gas, rather, it is combined with other elements as in water and organic molecules. Therefore, an extensive use of hydrogen as fuel (as it is usually called - the hydrogen economy) relies on the development of efficient hydrogen production means [1]. Another hurdle, that should be overcome in order to make the use of hydrogen fuel feasible, is that of hydrogen storage [1, 2]. This is the main topic of the present thesis.

A hydrogen storage system suitable for mobile applications must meet simultaneously the following six requirements set up based on economical and environmental considerations [3]:

- (i) high gravimetric (>4.5 wt%) and volumetric (> 36 g H_2 /L) densities,
- (ii) the operation temperature approximately in the range 60 – $120^\circ C$.
- (iii) reversibility of the thermal absorption/desorption cycle,
- (iv) low cost,
- (v) low-toxicity and
- (vi) safety.

A promising prospective approach to achieving this goal is the solid-state storage where H atoms are stored in the lattice of a host material. This method is motivated by the fact that hydrogen storage in gaseous form under high-pressure or in liquid state are not sufficiently efficient. Besides the concerns on safety and costs in compressing and liquifying the hydrogen gas, the energy density of hydrogen gas under 700 bar (4.4 MJ/L) and liquid hydrogen at 20K (8 MJ/L) are smaller than that in gasoline. The hydrogenation-dehydrogenation processes in some transition metals like Nb and V take place at ambient conditions easily satisfying requirement (ii). However, the hydrogen gravimetric densities in these transition metals seldom exceed 3 wt% so that the requirement (i) is not fulfilled. In fact, for a material to store more than 6 wt% of hydrogen it has to be made of light elements. Therefore, a great deal of research has turned to investigate light metal hydrides (LMH) like alanates ($KAlH_4$, $NaAlH_4$, $LiAlH_4$, etc.), borates (KBH_4 , $NaBH_4$ and $LiBH_4$, etc.), amide-imide ($LiNH_2$ - Li_2NH) [4] and saline hydrides (MgH_2) [2]. These materials display high storage capacity reaching up to 18 wt% in $LiBH_4$. However, in these compounds H atoms are held by strong ionic and co-

valent bonds resulting in unfavorable thermodynamics and slow kinetics for the hydrogen sorption reactions. Nevertheless, they are still being considered as good candidates thanks to the development of new methods to destabilize them.

In fact, to improve hydrogen storage properties of LMH the following approaches are currently being pursued: addition of catalysts, synthesis of nano-particles and mixture of different hydride phases. In this thesis, we deal with different problems related to these three approaches by employing first-principles calculations. We have investigated for instance the effect of impurities on hydrogen desorption in NaAlH_4 , NaBH_4 and MgH_2 nano-cluster, and also the thermodynamics of hydrogen sorption reactions in Li-Mg-N-H systems where the fully hydrogenated state consist of a mixture of $\text{Mg}(\text{NH}_2)_2$ and LiH .

Another alternative approach to store hydrogen in solid state systems consist on adsorbing hydrogen molecules on the surface of materials in a non-dissociative manner. One important advantage of this approach is that the kinetics of H-loading and releasing is fast, which is due to the fact that no chemical bond reconstruction takes place. However, since the hydrogen molecules are held by weak van der Waals forces, cryogenic temperatures are required in order to keep the tank loaded. There are many materials with high surface areas that are able of storing significant amount of hydrogen in this way, e.g. carbon nanotubes [5], molecular clathrates [6] and metal-organic frameworks [7]. In the present thesis, we have investigated in particular the hydrogen storage properties of the metal-organic frameworks.

Besides the use for hydrogen storage, the metal-hydrogen systems are also considered as good candidates for other technological applications thanks to the significant changes in the physical properties of the host compound induced by the presence of hydrogen [8]. For instance, the hydrogenation of Mg leads to a metal-insulator transition with the system changing from the shining metallic state (Mg) to a wide band-gap semiconductor (transparent) state (MgH_2). Such switchable optical properties motivated the application of these materials for the so-called *smart* windows. This is also the motivation for our investigations on the optical properties of different phases of MgH_2 .

The properties of the metal hydrides can be further tuned by utilizing phase transitions triggered by a change in pressure and/or temperature. The understanding of the underlying physics of these phenomena is important from fundamental and applied points of view. We have studied such phase transitions in three important hydride systems, namely NaBH_4 , Li_2NH and ErH_3 .

The outline of this thesis is as follows. In chapter 2, the basic concepts of the general theoretical background used for most of the works are reviewed. The subsequent chapters contain the summaries of the results along with some specific background information in the following sequence: chapter 3 - hydrogen storage properties of the chemical hydrides, chapter 4 - hydrogen storage properties of metal-organic frameworks; chapter 5 - structural phase transformation induced by pressure and temperature; and chapter 6- optical properties of saline hydrides. The conclusions and outlook are presented on chapter 7.

2. Theoretical background

In this chapter, the basic concepts of the general theoretical background used for most of the works in this thesis are presented. Firstly, the foundations of density functional theory and of the computational methods used in its implementations are described. After that, in sections 2.3, the basis for the calculation of atomic forces along with a brief discussion about the process of geometry optimization will be provided. Lastly, in section 2.4, the basic concepts of *ab initio* molecular dynamics are described.

2.1 Density Functional theory

2.1.1 The many-body problem

In order to study the properties of an interacting electron-nucleus system, containing n electrons and t nuclei, one has to solve the Schrödinger equation

$$H_t \Psi(\mathbf{r}_1, \mathbf{r}_2, \dots, \mathbf{r}_n, \mathbf{R}_1, \mathbf{R}_2, \dots, \mathbf{R}_t) = E_{tot} \Psi(\mathbf{r}_1, \mathbf{r}_2, \dots, \mathbf{r}_n, \mathbf{R}_1, \mathbf{R}_2, \dots, \mathbf{R}_t) \quad (2.1)$$

with the Hamiltonian

$$H_t = - \sum_i \frac{\hbar^2}{2m} \nabla_i^2 - \sum_I \frac{\hbar^2}{2M_I} \nabla_I^2 + \frac{1}{2} \sum_{i \neq j} \frac{e^2}{|\mathbf{r}_i - \mathbf{r}_j|} - \sum_{i,I} \frac{Z_I e^2}{|\mathbf{r}_i - \mathbf{R}_I|} + \frac{1}{2} \sum_{I \neq J} \frac{Z_I Z_J e^2}{|\mathbf{R}_I - \mathbf{R}_J|}. \quad (2.2)$$

The first and second terms in (2.2) correspond to the kinetic energy operators for the electrons and nuclei, respectively. The third, fourth and fifth terms are the potential operators that describe the electron-electron, electron-nucleus and nucleus-nucleus interactions, respectively. Although the Eq.(2.1), with the Hamiltonian (2.2), is written in an elegant and simple form, it can only be solved exactly for the hydrogen atom. Already for a helium atom, it requires approximation methods that are based on either the variational principle or perturbation theory. In a solid, where we have a complex many-body problem, the Eq.(2.1), with the Hamiltonian (2.2), becomes much more difficult to be solved requiring approximations that are usually done in three different levels.

The first approximation level, which is called the Born-Oppenheimer approximation, considers the nuclei frozen with the electrons in instantaneous equilibrium with them. Thus, the nuclei are treated as an external potential applied to the electron cloud. Such procedure is justified by the fact that the nuclei are much heavier than the electrons and consequently much slower. As a result, the total wave function can be written as the product of the electronic and ionic wave functions, with the electronic part being obtained by solving

the following Schödinger equation

$$H_e \psi_e(\mathbf{r}_1, \mathbf{r}_2, \dots, \mathbf{r}_n; \mathbf{R}_1, \mathbf{R}_2, \dots, \mathbf{R}_m) = E_e \psi_e(\mathbf{r}_1, \mathbf{r}_2, \dots, \mathbf{r}_n; \mathbf{R}_1, \mathbf{R}_2, \dots, \mathbf{R}_m), \quad (2.3)$$

with the electronic Hamiltonian given by

$$H_e = - \sum_i \frac{\hbar^2}{2m} \nabla_i^2 + \frac{1}{2} \sum_{i \neq j} \frac{e^2}{|\mathbf{r}_i - \mathbf{r}_j|} - \frac{1}{2} \sum_{i,I} \frac{Z_I e^2}{|\mathbf{r}_i - \mathbf{R}_I|}. \quad (2.4)$$

Within this approximation the complexity of the system is significantly reduced. However, the problem is still too difficult to be solved due to the electron-electron interaction (represented by the second term of the Hamiltonian in (2.4)). Therefore, it is still needed further approximations in order to reduce the Eq.(2.3) to a treatable form. Many approaches have been developed in order to accomplish such task as for instance the Hartree-Fock method and the Density Functional Theory (DFT). In this thesis, we have used only the latter, which is explained in the following sections.

2.1.2 The Hohenberg-Kohn theorems

The DFT is based on the theorems formulated by Hohenberg and Kohn (HK) [9]:

Theorem 1: For any system of interacting particles in an external potential $V_{ext}(\mathbf{r})$, there is an one-to-one correspondence between the potential and the ground-state particle density $\rho_0(\mathbf{r})$. The ground-state expectation value of any observable is, thus, a unique functional of the ground-state particle density $\rho_0(\mathbf{r})$

$$\langle \psi | A | \psi \rangle = A[\rho_0(\mathbf{r})]. \quad (2.5)$$

Theorem 2: For any external potential applied to an interacting particle system, it is possible to define an universal total energy functional of the particle density, which is written as

$$E[\rho(\mathbf{r})] = E_{HK}[\rho(\mathbf{r})] + \int V_{ext}(\mathbf{r}) \rho(\mathbf{r}) d\mathbf{r}, \quad (2.6)$$

where the term $E_{HK}[\rho(\mathbf{r})]$ includes all internal energies of the interacting particle systems. The global minimum of the functional in (2.6) is the exact ground-state total energy of the system E_0 and the particle density that minimizes this functional is the exact ground-state density $\rho_0(\mathbf{r})$, i.e.

$$\frac{\delta}{\delta \rho} E[\rho(\mathbf{r})] |_{\rho=\rho_0} = 0, \quad (2.7)$$

with

$$E_0 = E[\rho_0(\mathbf{r})]. \quad (2.8)$$

Here, we are not going to prove these theorems, but only discuss briefly some of their implications. The first theorem can be understood as follows. By knowing the ground-state particle density it is possible to reconstruct the system Hamiltonian and, by solving the Schrödinger equation, to calculate the many-body wave function. Therefore, all observable quantities can be obtained in a unique way from the particle density only. In other words, they can be written as functional of the density. It means that the density has as much information as the wave function does. In spite of the motivation brought by this theorem, we are still facing the same difficulties of our many-body problem.

The second theorem firstly states the total energy functional universality. The term E_{HK} , by construction, does not contain any information about the type of nuclei or their positions, and therefore it is an universal functional for the interacting electron system; and additionally, the contribution from the external potential to the total energy can be calculated exactly, since the density operator is known.

The second and probably the most important part of the second theorem is the variational principle. The total energy functional has a global minimum, which is the exact total energy of the ground-state. Moreover, out of many possible electron densities, the one that minimizes the total energy functional is the exact ground-state density corresponding to the external potential. This result provides a clue in finding a way to replace the original formulation of the many-body problem (Eq.(2.3)) by something that is more easily treatable. However, it can only be used if the functional E_{HK} is known (or a good approximation for it). The accomplishment of such task it will be presented in the next section.

2.1.3 The Kohn-Sham ansatz

Kohn and Sham (K-S) have developed a framework within which the H-K theorems can be applied for practical problems [10]. The main idea consists in replacing the interacting many-body problem by a corresponding non-interacting particle system in an appropriate external potential. In the K-S ansatz, the total energy functional in atomic units can be written as

$$E[\rho(\mathbf{r})] = T_0[\rho] + \frac{1}{2} \iint \frac{\rho(\mathbf{r})\rho(\mathbf{r}')}{|\mathbf{r} - \mathbf{r}'|} d\mathbf{r}d\mathbf{r}' + \int V_{ext}(\mathbf{r})\rho(\mathbf{r})d\mathbf{r} + E_{xc}[\rho(\mathbf{r})] + E_H, \quad (2.9)$$

which is the so-called Kohn-Sham functional. The first, second and third terms in (2.9) are the functionals for the kinetic energy of a non-interacting electron gas, the classical Coulomb contribution (Hartree term) for the electron-electron interaction and the external potential contribution due to nuclei and any other external potential, respectively. All many-body effects of exchange and correlation are incorporated into the term $E_{xc}[\rho(\mathbf{r})]$, which is called the exchange-correlation functional. The analytical expression of this term is unknown and the implementation of the K-S approach relies on our ability to

find a good approximation for it. The term E_{II} is the energy contribution from the interaction between the nuclei.

The construction of the Kohn-Sham functional is based on the assumption that the exact ground-state density can be represented by the ground-state density of an auxiliary system of non-interacting particles. Thus, one should interpret the K-S functional as the total energy functional of a non-interacting particle electron gas subject to two external potentials. One due to the nuclei and one due to the exchange-correlation effects.

According to the second theorem, the solution of the Kohn-Sham auxiliary system can be viewed as the minimization problem of the K-S functional with respect to the density $\rho(\mathbf{r})$, which leads to the following Schrödinger-like equation [10]

$$\left[-\frac{1}{2}\nabla^2 + V_{eff}(\mathbf{r}) \right] \psi_q(\mathbf{r}) = \varepsilon_q \psi_q(\mathbf{r}), \quad (2.10)$$

where ε_q are the eigenvalues, $\psi_q(\mathbf{r})$ are the K-S orbitals and $V_{eff}(\mathbf{r})$ is the effective potential,

$$V_{eff}(\mathbf{r}) = V_{ext} + \int \frac{\rho(\mathbf{r}')}{|\mathbf{r} - \mathbf{r}'|} d\mathbf{r}' + V_{xc}, \quad (2.11)$$

with the exchange-correlation potential defined by

$$V_{xc} = \frac{\delta E_{xc}[\rho]}{\delta \rho(\mathbf{r})}. \quad (2.12)$$

By construction, the exact ground-state density, $\rho(\mathbf{r})$, of a N-electron system is given by

$$\rho(\mathbf{r}) = \sum_q |\psi_q(\mathbf{r})|^2. \quad (2.13)$$

It should be pointed out that the K-S orbitals, $\psi_q(\mathbf{r})$, are not the wave function of electrons. They describe mathematical quasi-particles without physical meaning. Only the overall density of such particles is equal to the true electron density.

Assuming that the exchange-correlation potential defined in (2.12) is known, the exact ground-state density and energy of the many-body electron problem can be found by solving the single-particle K-S equations. In Eq. (2.10) the effective potential depends on the electron density $\rho(\mathbf{r})$, which depends on the K-S orbitals $\psi_q(\mathbf{r})$, which are being searched. It means that the K-S equations have to be solved iteratively until a self-consistent solution being reached.

2.1.4 Exchange-correlation functional approximations

The task of finding a good approximation for the exchange-correlation functional $E_{xc}[\rho(\mathbf{r})]$ is the main challenge in the implementation of the K-S scheme. In respect of that, many approaches have been proposed, among which the Local Density Approximation (LDA) [10] has been the most commonly used. The LDA exchange-correlation functional is written as

$$E_{xc}[\rho(\mathbf{r})] = \int \rho(\mathbf{r}) \epsilon_{xc}[\rho(\mathbf{r})] d\mathbf{r}, \quad (2.14)$$

where $\epsilon_{xc}[\rho(\mathbf{r})]$ is the exchange-correlation energy density of a homogeneous electron gas with the density $\rho = \rho(\mathbf{r})$. Thus, once one has assumed this approximation, the only information needed is the exchange-correlation energy of the homogeneous electron gas as a function of density. The exchange energy of a homogenous gas is well known to have a simple analytical form [11] and the correlation energy has been calculated with good accuracy within the quantum Monte Carlo method [12]. The LDA is expected to work well for systems with a slowly varying density, as for instance the nearly-free-electron metals. Surprisingly, it also appears to be successful for many other systems including semiconductors and insulators. However, further improvements are still required.

A natural way to improve the LDA is to consider the exchange-correlation energy density not only depending on the density $\rho(\mathbf{r})$ but also on its gradient $\nabla\rho(\mathbf{r})$. This is implemented through an approach called generalized gradient approximation (GGA). The most widely used parametrizations for the GGA-functional are those obtained by Becke (B88) [13], by Perdew and Wang (PW91) [14], by Perdew, Burke and Enzerhof (PBE) [15]. More recent developments of the exchange-correlation functionals include, besides the electron density and its gradient, the Kohn-Sham orbital kinetic energy. These new functionals are termed meta-GGA. In the studies on MgH_2 nanoclusters, the meta-GGA functional developed by Tao, Perdew, Staroverov and Scuseria (TPSS) [16] was employed.

2.2 Computational methods

In this section, the computational methods developed to solve Kohn-Sham equations, that have been used in this thesis, will be described. Here, the aim is to provide to the reader an understanding of the basic concepts but not to elaborate in-depth about technical details related to computational implementations.

2.2.1 The secular equation

In most of the known methods, to solve the Eq. (2.10) corresponds to find a set of coefficients $\{c_j^q\}$ needed to expand the K-S orbitals $\psi_q(\mathbf{r})$ in a given basis

set $\{\xi_j(\mathbf{r})\}$ such as

$$\psi_q(\mathbf{r}) = \sum_{j=1}^J c_j^q \xi_j(\mathbf{r}). \quad (2.15)$$

The K-S orbitals belong to an infinite function space (the Hilbert space), and therefore J should be infinite. However, in practice one always uses a limited basis set, which means that $\psi_q(\mathbf{r})$ is never exactly described.

Once we have chosen the basis set $\{\xi_j(\mathbf{r})\}$, with finite J , we can rewrite Eq. (2.10) as

$$\sum_{j=1}^J c_j^q \left[-\frac{1}{2} \nabla^2 + V_{eff}(\mathbf{r}) \right] \xi_j(\mathbf{r}) = \sum_{j=1}^J c_j^q \epsilon_q \xi_j(\mathbf{r}). \quad (2.16)$$

Multiplying from the left by the conjugate of the basis functions, $\xi_k^*(\mathbf{r})$ with $k = 1, \dots, J$, and integrating over all real space, we find

$$\sum_{j=1}^J c_j^q \int \xi_k^*(\mathbf{r}) \left[-\frac{1}{2} \nabla^2 + V_{eff}(\mathbf{r}) \right] \xi_j(\mathbf{r}) d\mathbf{r} = \sum_{j=1}^J c_j^q \epsilon_q \int \xi_k^*(\mathbf{r}) \xi_j(\mathbf{r}) d\mathbf{r}, \quad (2.17)$$

where $\int \xi_k^*(\mathbf{r}) \left[-\frac{1}{2} \nabla^2 + V_{eff}(\mathbf{r}) \right] \xi_j(\mathbf{r}) d\mathbf{r}$ are the matrix elements of the K-S single particle Hamiltonian in the basis states and $\int \xi_k^*(\mathbf{r}) \xi_j(\mathbf{r}) d\mathbf{r}$ are the overlap matrix elements. The solution of Eq. (2.17) gives rise to J eigenvalues and J set of coefficients $\{c_j^q\}$ that expand each of the J eigenfunctions in the given basis. Larger J will improve the representation of the eigenfunctions, but the calculations will be more time-consuming. To find a basis set size that is not only acceptable for practical applications but also efficient to represent the eigenfunctions, is one of the main challenges in condensed matter theory. This task is the third approximation level that was mentioned in the beginning of section 2.1.1.

2.2.2 The Bloch electrons and plane wave basis set

For a solid state system, the effective potential in the K-S equation (2.10) has the periodicity of the crystalline lattice. Therefore, the K-S orbitals, $\psi_{\mathbf{k}}^n(\mathbf{r})$, can be written as a product of a function $u_{\mathbf{k}}^n(\mathbf{r})$ that has the periodicity of the lattice and a plane wave $e^{i\mathbf{k} \cdot \mathbf{r}}$ with \mathbf{k} being any vector in the first Brillouin zone, i.e.

$$\psi_{\mathbf{k}}^n(\mathbf{r}) = u_{\mathbf{k}}^n(\mathbf{r}) e^{i\mathbf{k} \cdot \mathbf{r}}. \quad (2.18)$$

This is the Bloch theorem [17]. If a plane wave basis set is used, the periodic function in (2.18) can be written as a sum over plane waves that have the same periodicity as it. Such plane waves are those ones corresponding to reciprocal lattice vectors. Thus, the expansion of $\psi_{\mathbf{k}}^n(\mathbf{r})$ in this basis set is

$$\psi_{\mathbf{k}}^n(\mathbf{r}) = \frac{1}{\sqrt{\Omega_{cell}}} \sum_j c_j^n(\mathbf{k}) e^{i(\mathbf{k} + \mathbf{K}_j) \cdot \mathbf{r}}, \quad (2.19)$$

where Ω_{cell} is the volume of the primitive cell, \mathbf{K}_j are the reciprocal lattice vectors and the parameter n is called band index. As it was discussed in the previous section, now we have to search for the coefficient set $\{c_j^n(\mathbf{k})\}$. It should be pointed out that this basis set is \mathbf{k} -dependent, i.e. the eigenstates $\psi_{\mathbf{k}}^n(\mathbf{r})$ corresponding to different \mathbf{k} vectors are represented by different basis sets. The plane wave basis set can be limited by setting all \mathbf{K} with $K \leq K_{max}$. This means that all reciprocal lattice vectors that are inside a sphere with radius K_{max} are taken into the basis set. It is more common to specify the free electron energy corresponding to K_{max} , which is called cut-off energy

$$E_{cut} = \frac{\hbar^2 K_{max}^2}{2m}. \quad (2.20)$$

By using this plane wave basis set the Eq. (2.17) becomes

$$\sum_{j'} H_{j,j'}(\mathbf{k}) c_{j'}^n(\mathbf{k}) = \epsilon_n(\mathbf{k}) c_j^n(\mathbf{k}), \quad (2.21)$$

where

$$H_{j,j'}(\mathbf{k}) = \frac{\hbar^2}{2m} |\mathbf{k} + \mathbf{K}_j| \delta_{j,j'} + V_{eff}(\mathbf{K}_j - \mathbf{K}_{j'}) \quad (2.22)$$

and

$$V_{eff}(\mathbf{K}_j - \mathbf{K}_{j'}) = \int_{\Omega_{cell}} V_{eff}(\mathbf{r}) e^{i(\mathbf{K}_j - \mathbf{K}_{j'}) \cdot \mathbf{r}}. \quad (2.23)$$

The first term on the right-hand side of (2.22) is the matrix element of the kinetic energy operator, which assumes this form because of the plane wave basis functions orthonormality. The second term is the matrix element of the effective potential, which must be calculated according to Eq. (2.23).

The diagonalization of Hamiltonian (2.22) will give rise to a discrete set of eigenvalues and corresponding eigenfunctions labeled by n at each \mathbf{k} -point. It means that each eigenstate is uniquely labeled by both n and \mathbf{k} . For large volumes Ω , the \mathbf{k} -points densely sample the Brillouin zone and the eigenvalues $\epsilon_n(\mathbf{k})$ becomes continuous bands. Furthermore, all unique solutions are given by \mathbf{k} in the first Brillouin zone.

2.2.3 LAPW method

Let us start this section by discussing the efficiency of the plane wave basis set to describe solid state eigenfunctions. Let us do that by using the example presented in Ref. [18]. In order to represent in real space a wavefunction that oscillates within an interval of 0-0.1Å (which is the case of 3s electron in Ca) by a plane wave basis set, it is necessary to use plane waves with a period as small as roughly 0.01Å. Thus, we should set $K_{max} = 6.3 \times 10^{12} m^{-1}$. The volume of a sphere with this radius is around $10^{38} m^{-3}$. Dividing this volume by the volume of the first Brillouin zone of a cubic lattice with a lattice constant of 3Å (which is $9.2 \times 10^{30} m^{-3}$) and by considering that there is one lattice vector

K_j per Brillouin zone, we see that around 10^8 plane waves are needed. That would require diagonalization of $10^8 \times 10^8$ matrices. This is a task undoable even for supercomputers. Therefore, it is necessary to either find another basis set or replace this rapidly oscillating wavefunction by a smoother function.

The oscillating part of the wavefunctions occur in the inner region close to the nucleus (usually called atomic core), where the electrons behave pretty much as in the free atoms, i.e. they do not take part in the chemical bonds. Thus, one way to diminish the number of basis functions is to split the basis set into two distinct classes where the basis functions close to the nucleus are more similar to atomic orbitals. This is the idea behind the augmented plane wave method (APW) [18] originally developed by Slater [19]. In this method the crystal lattice is divided into two main parts, which are termed muffin-tin (MT) and interstitial (I) regions. The former consist of non-overlapping atomic sphere centered around each atomic site, while the latter is composed by all remaining space. Inside the muffin-tin region, the basis functions are linear combination of solutions of the Schrödinger equation for a spherical potential

$$\phi_{MT}(\mathbf{r}) = \sum_{lm} A_{lm} u_l(r, E_l) Y_m^l(\hat{\mathbf{r}}), \quad (2.24)$$

where l and m are the angular momentum quantum number, $Y_m^l(\hat{\mathbf{r}})$ are spherical harmonics and the function $u_l(r, E_l)$ satisfy the radial Schrödinger equation

$$-\frac{1}{2r^2} \frac{d}{dr} \left[r^2 \frac{du_l}{dr} \right] + \left[\frac{l(l+1)}{2r^2} + V(r) \right] u_l = E u_l. \quad (2.25)$$

In the interstitial region, the functions that are solution of the Schrödinger equation for a constant potential are plane waves, $\phi_I(\mathbf{r}) = \frac{1}{\sqrt{\Omega}} e^{i\mathbf{k} \cdot \mathbf{r}}$. Thus, APW basis functions are given by

$$\phi(\mathbf{r}, \mathbf{k}) = \begin{cases} \sum_{lm} A_{lm} u_l(r, E_l) Y_{lm}(\hat{\mathbf{r}}) & \mathbf{r} \in MT \\ \frac{1}{\sqrt{\Omega}} e^{i\mathbf{k} \cdot \mathbf{r}} & \mathbf{r} \in I \end{cases},$$

where the coefficients A_{lm} are determined by the boundary condition that the basis functions are continuous between MT and I regions.

The fact that APW basis functions are energy dependent could lead to unphysical results especially when the functions inside the MT region changes rapidly with energy. To overcome this limitation a method was proposed, which is called linearized augmented plane wave (LAPW) [20, 21]. Here the function u_l is replaced by the linear part of its expansion around a fixed energy E_p . Hence, the LAPW basis functions are given by

$$\phi(\mathbf{r}, \mathbf{k}) = \begin{cases} \sum_{lm} [A_{lm} u_l(r, E_p) + B_{lm} \dot{u}_l(r, E_p)] Y_{lm}(\hat{\mathbf{r}}) & \mathbf{r} \in MT \\ \frac{1}{\sqrt{\Omega}} e^{i\mathbf{k} \cdot \mathbf{r}} & \mathbf{r} \in I \end{cases},$$

where the coefficients A_{lm} and B_{lm} are determined by matching each basis function both in value and derivative at the MT boundary. Now, the basis functions are energy independent.

If no geometrical approximations are applied to the symmetry of the potential the method is called a full potential (FP) method. The results presented for electronic and optical properties of the high pressure phases of magnesium dihydride were calculated using the FP-LAPW method as implemented in the WIEN2k code [22].

2.2.4 PAW method

In most of the studies of this thesis, the electronic structure calculations and geometry optimizations have been performed using the projector augmented wave (PAW) method [23] as implemented in the Vienna *ab initio* simulation package (VASP) [24]. The PAW method is an all-electron frozen core method, which combines the features of both the ultra-soft pseudopotentials [25] and augmented plane wave methods [18]. Following the latter, the wavefunctions have a dual representation. Within spheres centered at each atomic position (the augmentation region) they are expanded by partial-waves and outside they are expanded into plane waves or some other convenient basis set.

The PAW method is based on the linear transformation that relates the set of all-electron valence functions ψ_q to the smooth functions $\tilde{\psi}_q$, which is given by

$$|\psi_q\rangle = \tau |\tilde{\psi}_q\rangle. \quad (2.26)$$

The requirement that the transformation in (2.26) is linear leads to the following form for the operator τ

$$\tau = \hat{\mathbf{1}} + \sum_i (|\phi_i\rangle - |\tilde{\phi}_i\rangle) \langle \tilde{p}_i|. \quad (2.27)$$

and therefore the all-electron eigenstate can be written as

$$|\psi_q\rangle = |\tilde{\psi}_q\rangle + \sum_i (|\phi_i\rangle - |\tilde{\phi}_i\rangle) \langle \tilde{p}_i | \tilde{\psi}_q\rangle. \quad (2.28)$$

The ϕ_i is the all-electron partial wave, which is solution of the radial Schrödinger equation for the isolated atom. Therefore, the index i refers to the atomic site \mathbf{R} , the angular momentum quantum numbers $L = l, m$ and an additional index s referring to the reference energy $\epsilon_{s,l}$. The $\tilde{\phi}_i$ is the smooth partial-function, which is equal to ϕ_i outside the augmentation region. The projector state $\langle \tilde{p}_i |$ is dual to the state $|\tilde{\phi}_i\rangle$, satisfying the condition

$$\langle \tilde{p}_i | \tilde{\phi}_j \rangle = \delta_{i,j}, \quad (2.29)$$

with i and j belonging to the same augmentation sphere.

For any operator \hat{A} in the all-electron problem, it is possible to introduce a transformed operator \tilde{A} that operates on the smooth part of the wave function such as

$$\tilde{A} = \tau^\dagger \hat{A} \tau = \hat{A} + \sum_{i,j} |\tilde{p}_i\rangle \langle \phi_i | \hat{A} | \phi_j \rangle - \langle \tilde{\phi}_i | \hat{A} | \tilde{\phi}_j \rangle \langle \tilde{p}_j|. \quad (2.30)$$

Moreover, one can add a term of the form

$$\hat{B} - \sum_{i,j} |\tilde{p}_i\rangle \langle \tilde{\phi}_i | \hat{B} | \tilde{\phi}_j \rangle \langle \tilde{p}_j| \quad (2.31)$$

to right-hand side of Eq. (2.30), where \hat{B} is an arbitrary operator that is localized within the augmentation regions. The expectation value of this operator is zero for any smooth function $\tilde{\psi}$. The Kohn-Sham equation is, thus, transformed as

$$\tau^\dagger \hat{H} \tau | \tilde{\psi}_q \rangle = \varepsilon_q \tau^\dagger \tau | \tilde{\psi}_q \rangle. \quad (2.32)$$

The physical quantities can be obtained following the description given in Eq. (2.30). For instance, the all-electron charge density is given by

$$n(\mathbf{r}) = \tilde{n}(\mathbf{r}) + n^1(\mathbf{r}) - \tilde{n}^1(\mathbf{r}) \quad (2.33)$$

where

$$\tilde{n}(\mathbf{r}) = \sum_q f_q \langle \tilde{\psi}_q | \mathbf{r} \rangle \langle \mathbf{r} | \tilde{\psi}_q \rangle, \quad (2.34)$$

$$n^1(\mathbf{r}) = \sum_{q,(i,j)} f_q \langle \tilde{\psi}_q | \tilde{p}_i \rangle \langle \phi_i | \mathbf{r} \rangle \langle \mathbf{r} | \phi_j \rangle \langle \tilde{p}_j | \tilde{\psi}_q \rangle \quad (2.35)$$

and

$$\tilde{n}^1(\mathbf{r}) = \sum_{q,(i,j)} f_q \langle \tilde{\psi}_q | \tilde{p}_i \rangle \langle \tilde{\phi}_i | \mathbf{r} \rangle \langle \mathbf{r} | \tilde{\phi}_j \rangle \langle \tilde{p}_j | \tilde{\psi}_q \rangle. \quad (2.36)$$

The last two terms $n^1(\mathbf{r})$ and $\tilde{n}^1(\mathbf{r})$ are localized around each atom and they contain contributions from the core and smooth core states, respectively. In practice, the smooth core density is constructed instead of constructing a smooth core state for each core state individually unless one is interested in the physical properties that are related to the core states.

From Eq. (2.30), one can also write the all-electron functional for the total energy as

$$E = \tilde{E} + E^1 - \tilde{E}^1 \quad (2.37)$$

where \tilde{E} is a smooth part, which is calculated on a regular grid in Fourier or real space, and E^1 and \tilde{E}^1 are two on-site contributions that are calculated on a radial grid in an angular momentum representation.

If the partial and the plane wave basis set, which are used to provide the dual representation of $\tilde{\psi}$ and ψ , satisfies the completeness condition then the PAW method is an exact implementation of the density functional theory within the frozen core approximation. However, in practice one always uses a finite basis set as we have already mentioned in the section 2.2.1. Here, it means that the plane waves are included only up to a given cutoff energy and the number of all electron partial waves ϕ_i , pseudo-partial waves $\tilde{\phi}_j$ and projectors is finite. Therefore, the convergency of the results have to be checked with respect to the plane-wave cutoff and/or the number of partial waves.

2.2.5 Localized basis set

In the LAPW method the Kohn-Sham orbitals are expanded by two different kinds of basis functions, plane waves in the interstitial and functions that are more similar to atomic orbitals in the muffin-tin region. This is done to improve efficiency of the basis set composed only of plane waves. An alternative approach, that has experienced a significant growth in condensed matter and is the one used for atoms and molecules, is to use only localized atomic orbital-like basis functions, which can be for instance of Gaussian form, Slater-type orbitals or numerical radial atomic like orbitals [11].

With the considerations that the basis set should be as efficient as possible, in the sense that the expansion of Kohn-Sham orbitals requires the fewest possible terms, and also that it should be fast in the evaluation of Hamiltonian matrix elements, the basis set of choice in quantum chemistry is composed of contracted Gaussian functions (CGF) [26]. In this case, each basis function is a linear combination (contraction) of Gaussian functions (primitives). The significant advantage is that the integrals involving such functions reduces to the sum of integrals involving primitive Gaussian functions, which are much simpler to be solved. Thus, the basis functions are written as

$$\phi_{\mu}^{CGF}(\mathbf{r} - \mathbf{R}_A) = \sum_{p=1}^L d_{p\mu} g_p(\alpha_{p\mu}, \mathbf{r} - \mathbf{R}_P), \quad (2.38)$$

where L is the length of the contraction and $\alpha_{p\mu}$ and $d_{p\mu}$ are the contraction exponents and coefficients, respectively. These parameters are chosen so that the CGF basis function has some desired properties. In (2.38) $g_p(\alpha_{p\mu}, \mathbf{r} - \mathbf{R}_P)$ are the normalized primitive Gaussian functions centered at \mathbf{R}_P , which are of $1s, 2p, 3d, \dots$ type. For more details about their functional forms see Ref. [26].

The method that uses contractions of L primitive Gaussians for each basis function and also has the contraction coefficients and exponents optimized so that the basis functions approximate the Slater functions is termed STO-LG. Specifically, STO-3G has become the standard for minimal basis calculations. The term "minimal" means the least number of basis functions required to describe the occupied atomic orbitals. Even though this basis allows calculations of large systems, the calculated properties can display significant discrepancy from the experimental observations. The next step toward improving the re-

sults is to use a basis with two, three, four, ... functions for each minimal basis function which is known as double zeta (DZ), triple zeta (TZ), quadruple zeta (QZ), ... basis set. There are basis sets where only the valence functions are, for instance, doubled while a single function is used for the inner shell orbitals. These are called split valence basis sets. Further improvement can also be achieved by adding polarization functions, i.e., adding *d*-type functions for the atoms of the first row of periodic table and *p*-type functions to H. It should be pointed out that the choice of the best basis set that provides a good compromise between accuracy and computational time will depend on the system and properties under investigation.

In the investigation of MgH₂ nano-cluster presented in Paper I, we have used for Mg atoms a split-valence polarization (SVP) basis with extra *d*-functions, which was optimized for metallic Mg clusters [27]. The other atoms were treated with standard SVP basis sets implemented in Turbomole code [28].

So far, the basis of Density Functional Theory and of the methods used for its implementation were presented. Once one has obtained a solution to the K-S equation, the total energies, forces and other quantities that characterize the systems can be evaluated. In the next section, the theoretical basis for the calculation of forces are described along with a brief discuss about the process of geometry optimization. Thereafter, in section 2.4, the basic concepts of the *ab initio* molecular dynamics used in this thesis are presented.

2.3 Force theorem and geometry optimization

In this section, geometry optimization is briefly discussed, i.e. the search for the spatial equilibrium configuration in which the atoms are arranged in the ground-state. In the solid state, besides the atomic positions, the shape and volume of the unit cell must be optimized as well.

An atom feeling a net force moves in the direction of the force so that the total energy is minimized. The equilibrium configuration is reached when all such forces are equal to zero, or more realistic, when they are within some convergence criterion. These forces are calculated by using the force theorem or, as it is usually called, the Hellmann-Feynman theorem [11]. This theorem can be understood as follows. The forces due to the atomic displacements can be written as

$$\mathbf{F}_l = -\frac{\partial E}{\partial \mathbf{R}_l}, \quad (2.39)$$

where E is the system total energy,

$$E = \frac{\langle \Psi | H | \Psi \rangle}{\langle \Psi | \Psi \rangle}. \quad (2.40)$$

Thus, assuming $\langle \Psi | \Psi \rangle = 1$ and substituting (2.40) into (2.39) we get

$$\mathbf{F}_I = -\langle \Psi | \frac{\partial H}{\partial \mathbf{R}_I} | \Psi \rangle - \langle \frac{\partial \Psi}{\partial \mathbf{R}_I} | H | \Psi \rangle - \langle \Psi | H | \frac{\partial \Psi}{\partial \mathbf{R}_I} \rangle. \quad (2.41)$$

At the exact ground-state solution the energy is extremal with respect to all possible variations of the wavefunction, and as a consequence the last two terms on the right hand side of (2.41) vanish. Therefore, the forces are determined exclusively by the terms explicitly dependent upon atomic positions and it can be written as

$$\mathbf{F}_I = -\frac{\partial \langle \Psi | H | \Psi \rangle}{\partial \mathbf{R}_I} = -\langle \Psi | \frac{\partial H}{\partial \mathbf{R}_I} | \Psi \rangle. \quad (2.42)$$

Thus, one can keep $|\Psi\rangle$ at their ground-state values and calculate the partial derivative of the total energy with respect to the ionic positions only.

There are two main factors that can affect the use of the force theorem. One is the errors due to non-self-consistency and another is the explicit dependence of the basis functions upon the ionic positions. The latter gives rise to the so-called Pulay forces. These factors must be treated explicitly in order to avoid additional errors. A good discussion can be found in Ref. [11]. For a plane wave basis set the Pulay forces are zero because the basis functions do not depend on the atomic position. However, in this case, one still needs to be careful if the volume and shape of a unit cell are being optimized. It is necessary to guarantee that the plane wave basis set is complete. In practice, this is done by using a large energy cutoff.

2.4 Molecular dynamics

The dynamics of classical objects is governed by Newton's equation, which is written as

$$M_i \ddot{\mathbf{R}}_i = -\frac{\partial E}{\partial \mathbf{R}_i} = \mathbf{F}_i[\{\mathbf{R}_j\}], \quad (2.43)$$

where $E[\{\mathbf{R}_i\}]$ is the total interaction energy. This equation can be integrated in a discrete grid of time using for instance the Verlet algorithm. The main advantage of this integrator is that the energy is conserved and the simulations are stable for long runs.

The molecular dynamics (MD) simulations have experienced significant advances in the last two decades thanks to developments in both theoretical methods and computational facilities [11]. In the classical MD, which was the only possible approach in the past but still widely employed, the forces are obtained through effective potentials between nuclei (parameterized pair potentials) that attempt to include the effects of electrons. More recently, *ab initio* (or first-principles based) MD was made possible. In this case, the forces are determined directly from the solution of quantum mechanical problem of

electrons without any adjustment of parameters. However, the nuclei are still treated as classical objects with their dynamics governed by Eq. (2.43).

There are two main methods available to implement *ab initio* MD. The first (which is the one used in this thesis) divides the problem in two parts: (a) the motion of the nuclei and (b) the self-consistent solution of Kohn-Sham equations for the electrons. This methodology is termed Born-Oppenheimer molecular dynamics. The alternative approach is Car-Parinello MD where the dynamics of nuclei and the quantum electronic problem are solved within the same algorithm. A good comparison between these two implementations displaying their advantages and disadvantages can be found in Ref. [11]. However, it is worthwhile to highlight here the following features of the Born-Oppenheimer MD: (a) the nuclei dynamics determines the best choice for the time steps, unlike the Car-Parinello simulation where the time step is determined by the fictitious dynamics of the electrons; (b) the quantum electronic problem has to be solved accurately at each time step, which makes these steps more time-consuming than Car-Parinello MD; (c) there is unphysical leakage of the total energy that has to be carefully monitored.

The MD simulations can be used either to investigate the dynamics of the molecular systems or to calculate macroscopic properties. The latter is based on the ergodic hypothesis which claims that the time average of a observable obtained using the individual atomic trajectories should be the same as the ensemble average obtained using for instance Monte Carlo method (for more details see [29]). To perform such averaging, the system is initially equilibrated in a given thermodynamical state (equilibration step) and then extra runs are performed to store the desired trajectories used in the average evaluations (production steps). The thermodynamical state (i.e. the ensemble) can be fixed by using any triad of the following environmental variables: the number of particles N , volume of simulation box V , total energy E , temperature T , chemical potential μ . The most common ensembles are fixed by the following sets of variables: N, V , and E - microcanonical ensemble; N, V , and T - canonical ensemble; μ, V , and T - grand ensemble; N, P , and T - isothermal-isobaric ensemble.

From the simulated individual atomic positions as a function of time it is possible to compute the radial distribution function (RDF) $g(r)$, which measures how the atoms are organized in the vicinity of one another and thereby providing information about the local structures. This is an important *static* property provided by MD simulations that can also be extracted from x-ray and neutron diffraction measurements. For uniform substances the RDF is evaluated through the following expression

$$g(r) = \frac{\sum_{k=1}^M N_k(r, \Delta r)}{M(\frac{1}{2}N)\rho V(r, \Delta r)} \quad (2.44)$$

where $N_k(r, \Delta r)$ is the result of a counting operation at instant t_k in the run, which results in the number of atoms found in a spherical shell of radius r and thickness Δr with the shell centered in another atom. This quantity can also be

interpreted as a ratio of a local density to the system density ρ . In Eq. (2.44), M , N and $V(r, \Delta r)$ are the number of time steps, the number of particles in the simulation box and the volume of the spherical shell, respectively. In the probabilistic interpretation of the radial distribution function we have that

$$\frac{\rho}{N-1} g(r) V(r, \Delta r) \quad (2.45)$$

is the probability of finding an atom center in a spherical shell of radius r and thickness Δr with the shell centered on another atom. The radial distribution function gives us a good insight of how the presence of one atom affects the arrangement of the neighboring atoms. In this thesis, systems containing different kind of atoms in the same compound were studied. Therefore, the term pair distribution function was used to indicate that we are calculating the radial distribution function for a particular pair of atoms.

From the simulated individual atomic positions as a function of time it is also possible to extract dynamical properties of the system by evaluating the mean square displacement (msd), which is given by

$$msd = \left\langle \sum_i^N [r_i(t) - r_i(0)]^2 \right\rangle. \quad (2.46)$$

The msd is related to the diffusion coefficient D through the Einstein equation, which can be written as

$$D = \frac{1}{6N} \lim_{t \rightarrow \infty} \frac{d}{dt} \left\langle \sum_i^N [r_i(t) - r_i(0)]^2 \right\rangle, \quad (2.47)$$

where N is the number of particles in the simulation box.

3. Hydrogen storage I: Chemisorption

The understanding of the effect of both addition of catalysts and mixing of hydride phases on the hydrogen storage properties of chemical hydrides is an important requisite to design new materials for on-board hydrogen storage applications. In this chapter, the summaries of our studies on these topics are presented. In the first three sections some background information are introduced where a classification of the chemical hydrides according to the nature of their chemical bonds are provided followed by the description of the mechanism and thermodynamics of the hydrogen sorption reactions. The results are in Sections 3.4 and 3.5.

3.1 Chemical hydrides classification

Hydrogen reacts with many different elements forming a wide variety of compounds which are classified according to their chemical bonds. With alkali and alkaline earth elements hydrogen forms ionic compounds that are also called saline hydrides such as LiH , MgH_2 , BeH_2 , etc. Covalent hydrides are formed by Group III-V non-metallic elements as well as by light metals of Group I-IV. With transition metals, lanthanides and actinides hydrogen can form either metallic or semiconductor hydrides. These metals display electronegativities similar to hydrogen.

Another class of materials widely studied for application as hydrogen storage medium is the complex light metal hydrides (CLMH). In these materials hydrogen reacts with group IA, IIA and IIIA light metals to form complexes such as AlH_4^- , AlH_6^{3-} , BH_4^- , NH_2^- and NH_2^{2-} , which in turn form ionic bonds with alkali and alkaline earth metals to give rise to very stable hydrides, e.g. NaAlH_4 , Na_3AlH_6 , NaBH_4 , LiNH_2 and Li_2NH . An excellent description of the applications of complex light metal hydrides to hydrogen storage can be found in the review article by S. Orimo *et al.* [4].

3.2 Hydrogenation mechanism

In this section, we discuss shortly the possible events that can occur when the hydrogen gas interacts with a piece of metal to form the metal hydrides. This interaction may be described by the Lennard-Jones attractive-repulsive potential for hydrogen binding to a metal, as indicated in Ref. [30]. As the hydrogen molecules approach the metallic surfaces they face a potential energy

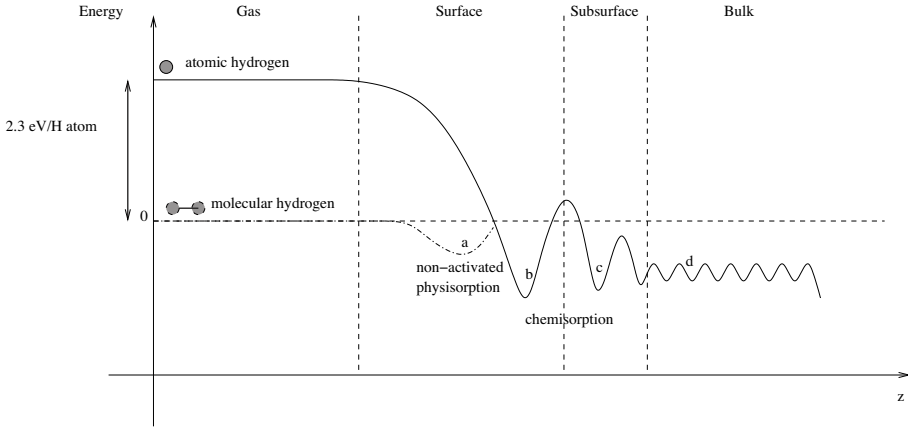


Figure 3.1: Qualitative illustration of the Lennard-Jones potential energy curve for hydrogen (in the atomic and molecular states) interacting with a metal where four different events are illustrated, namely (a) non-activated physisorption, (b) surface chemisorption (c) sub-surface chemisorption and (d) bulk chemisorption/diffusion. The potential energy curve for the molecular hydrogen is drawn only until it meets the potential energy curve for the atomic hydrogen. Adapted from Ref. [30].

profile with successive minima, which corresponds to molecular or atomic adsorption on the metal surface, atomic absorption on the sub-surface layers and bulk absorption, respectively. In Figure 3.1, we illustrate qualitatively such Lennard-Jones potential where we indicate the minimum corresponding to each event.

Depending on the temperature-pressure conditions H_2 molecules can either be trapped in a shallow potential well without being dissociated, a process denoted as physisorption, or be split, allowing hydrogen atoms to form new chemical bonds with the host metal, a process termed chemisorption. In the potential profile presented in Figure 3.1, the transition from molecular to atomic state does not face any energy barrier (i.e. the atomic and molecular curves cross each other at an energy point equal to or lower than the energy state of H_2 in the gas phase), and therefore, the chemisorption displays high statistical probability to take place and the physisorption is said to be non-activated. Let us further point out that there still exists the physisorption minimum, which may be populated at low temperature and low pressure by some of the H_2 molecules but with low statistical probability. To rise up this probability, and to extend it to higher temperatures and pressures, there must exist a finite energy barrier for the molecular-atomic transition. In this case, the physisorption would be said to be activated. This scenario will be further explored and discussed in the next Chapter.

As the dissociation of the molecules occurs, H atoms either stay on the surface (or sub-surface) or diffuse into the bulk populating interstitial sites. The interstitial hydrogen form initially a solid solution but as the concentration is increased, a new single-phase compound starts to be stabilized, the chemical

hydride. More detailed description of such mechanism can be found in Ref. [30].

3.3 Thermodynamics

The reaction



will become thermodynamically favorable when

$$\Delta G = G_{M_yH_x} - (yG_M + \frac{x}{2}G_{H_2}) \leq 0, \quad (3.2)$$

where ΔG is the Gibbs free energy, which can be written as

$$\Delta G = \Delta H - T\Delta S. \quad (3.3)$$

In Eq. (3.3), ΔH and ΔS are the reaction enthalpy and entropy, respectively. The former represents the heat released or absorbed at a constant pressure during the reaction and it is negative for the hydrogenation reaction. Therefore, for the dehydrogenation reaction to be thermodynamically favorable the value of $T\Delta S$ should be greater than that of ΔH . At a given pressure this is achieved by rising the temperature. It should be pointed out that even when the reaction is thermodynamically favorable, for a given temperature-pressure condition, energy barriers could make it kinetically unfavorable. This is the case, for instance, for the dissociation of $NaAlH_4$. An illustration of the overall reaction barrier is shown in Figure 3.2. As indicated in this sketch the presence of a catalyst affects the height of such a reaction barrier, which only affects the kinetics of the chemical reaction. To modify the thermodynamics of the reaction one has to employ approaches able to change the difference between the internal energies of the hydrogenated and dehydrogenated states. One currently used method is the mixing of hydride phases. This is the topic of the section 3.5. In the following, we further discuss the calculations of the thermodynamic functions.

For the solid-state phases, the enthalpy function can be written as

$$H(T, V) = U^{elec}(T, V) + U^{phonon}(T, V) + PV, \quad (3.4)$$

where $U^{elec}(T, V)$, $U^{phonon}(T, V)$, P and V are the electronic internal energy, internal energy of phonons, the external pressure and the molar volume, respectively. For solid-state materials at 1 atm, the value of PV term is usually very small compared to the other terms and can be neglected [31]. The phonon (or vibrational) internal energy is written as

$$U^{phonon}(V, T) = \frac{1}{2}r \int_0^\infty \hbar\omega g(\omega) \coth\left(\frac{\hbar\omega}{2k_B T}\right) d\omega, \quad (3.5)$$

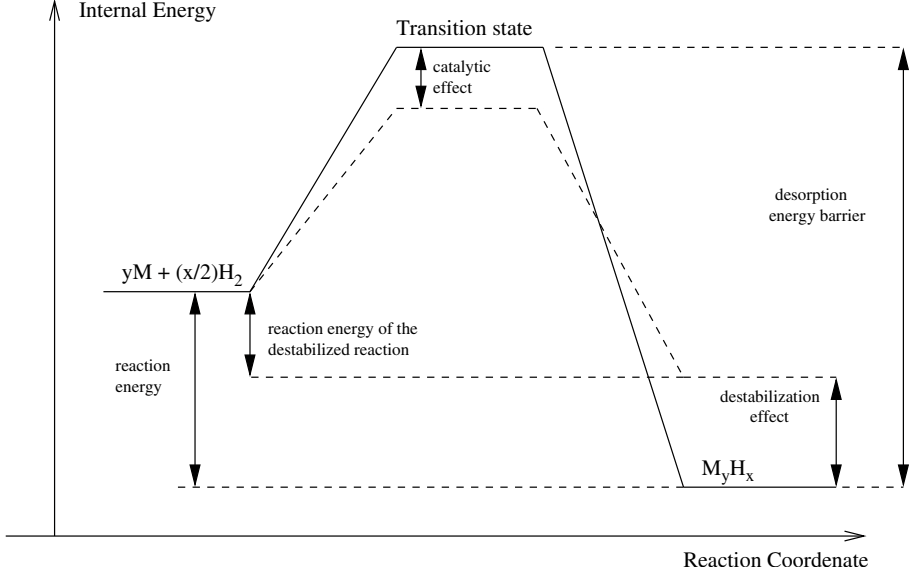


Figure 3.2: Illustration of an energy diagram for the hydrogen sorption reaction. Adapted from Ref. [30]

where $g(\omega)$ and r are the phonon density of states and the degrees of freedom of the unit cell, respectively. The internal energy depend on the cell volume through the vibration frequencies, which are volume dependent within the quasi-harmonic approximation. As the temperature tends to zero the vibration energy tends to a non-zero value (quantum mechanics effect), which is called zero point energy and is written as

$$E_{(ZP)}(V) = \lim_{T \rightarrow 0} U^{phonon}(T, V) = \frac{1}{2} r \int_0^\infty \hbar \omega g(\omega) d\omega. \quad (3.6)$$

In this thesis, $E_{(ZP)}(V)$ was calculated from discrete summation the vibrations frequencies obtained from diagonalization of the Hessian matrix at gamma point only. In some cases it was necessary to employ a supercell approach to converge the calculated values. Finally, the enthalpy at 0 K reduces to

$$H = E^{elec}(V) + E_{(ZP)}(V) + PV, \quad (3.7)$$

where $E^{elec}(V)$ is the electronic total energy at 0 K, which is calculated from first-principles. It was used here the following notation: $E^{elec}(V) = U^{elec}(0, V)$. The enthalpy function of hydrogen gas at 0 K is also calculated using Eq. (3.7). The calculated 0 K enthalpy of the hydriding reaction is shown to be sufficient to catch most of the trends.

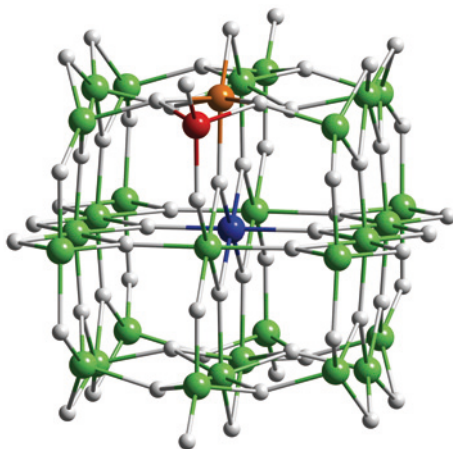


Figure 3.3: Ball-and-stick model of a MgH_2 cluster with 31 formula units. Mg atoms are colored in green and hydrogen atoms in white. Three different Mg sites where transition metal atoms are substituted are shown in red (edge site), orange (surface site) and blue (central site).

3.4 Role of catalysts on dehydrogenation

3.4.1 MgH_2 nanocluster

Among the saline hydrides MgH_2 is one of the most studied material for hydrogen storage mainly due to its high hydrogen content (7.6wt%) and low manufacturing cost. However, its slow hydrogen absorption/desorption kinetics and high dissociation temperature (nearly 300 °C) limit its practical applications [32]. In order to overcome these limitations much attention turned to investigate nanocrystalline structures and/or the addition of alloying elements [33]-[35]. It has been shown that mechanical ball milling can reduce the particle size to about 10 nm where defects, large surface areas, and grain boundaries help to improve the kinetics and thermodynamics of hydrogen sorption [36]. Further milling with transition metal additives such as Ti, V, Fe, Co, and Ni leads to greatly enhanced hydrogen sorption kinetics [34].

In Paper I, we have investigated the hydrogen storage properties of MgH_2 nanoclusters interacting with transition metal dopants. The calculations were carried out using DFT and contracted Gaussians basis sets. The $\text{Mg}_{31}\text{H}_{62}$ cluster was constructed by cutting out a portion of the MgH_2 bulk crystal structure and by rearranging some surface atoms in order to attain the desired Mg_nH_{2n} stoichiometry (see Figure 3.3). This study was performed by using the transition metal elements Ti, V, Fe, and Ni as dopants. The models for the fully dehydrogenated metal clusters were obtained by removing all hydrogen atoms from a fully relaxed metal hydride cluster and then performing geometry relaxation to form Mg_{31} cluster.

The substitutional doping is found to be energetically favorable for all elements in both MgH_2 and Mg clusters if the total energy of isolated atoms in

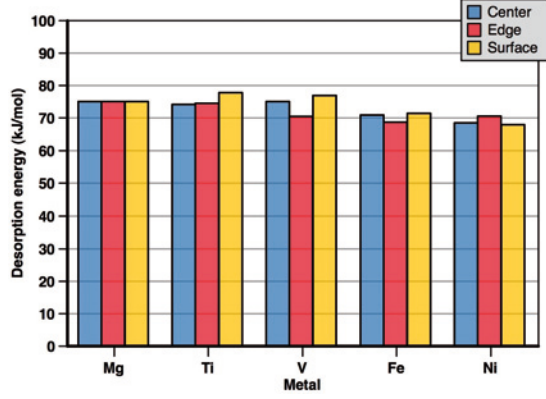
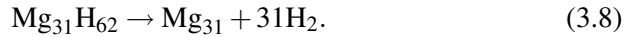


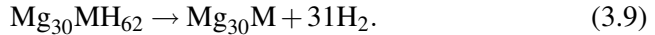
Figure 3.4: Average hydrogen desorption energies for $\text{Mg}_{30}\text{MH}_{62}$ clusters with dopants at three different sites as compared to a pure $\text{Mg}_{31}\text{H}_{62}$ cluster

the gas phase are taken as the chemical potentials. All studied elements are also found to prefer the surface sites over the bulk site for both hydrogenated and dehydrogenated clusters except for Ti in Mg cluster. Such preference for surface sites is consistent with the catalytic activity of these transition metals. The two surface sites considered here are named *surface* and *edge* sites and they are labeled, respectively, by the orange and red balls in Figure 3.3.

To investigate the effect of this small amount of alloying on the thermodynamics of the overall hydrogen desorption, we have calculated the energies of the following chemical reactions associated full dehydrogenation for both the pure and transition metal doped MgH_2 cluster, respectively:



and



where M represent the different transition metals used in this study. The reaction energies are calculated by taking into account only the electronic total energies of the different phases. These results are given in Figure 3.4. As can be observed, for all systems, the reaction energies fell in a range from 70 to 80 $\text{kJ} (\text{mol H}_2)^{-1}$ with the smallest values for Fe and Ni. Thus, the small amount of alloying elements (3.2 wt% in our case) does not affect much the thermodynamics of these reactions.

In order to estimate how much transition metals at the surface influence the removal energies of adjacent hydrogen atoms, we have calculated such energies for the *surface* and *edge* sites using the formula:

$$\Delta E = E_T(\text{Mg}_{30}\text{MH}_{61}) + 0.5E_T(\text{H}_2) - E_T(\text{Mg}_{30}\text{MH}_{62}). \quad (3.10)$$

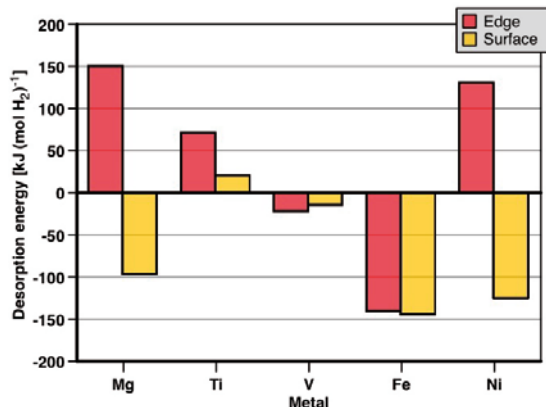


Figure 3.5: Single hydrogen desorption energies for $\text{Mg}_{30}\text{MH}_{62}$ clusters at two different surface sites.

The results are shown in Figure 3.5. In nanocluster MgH_2 , the removal of hydrogen bound to *edge* site atoms costs energy while the process is exothermic for the *surface* atom. This demonstrates that nanostructuring can indeed weaken the strength of the Mg-H bond even without the addition of catalysts. The H removal energies are also strongly affected by the presence of the impurities with the most extreme case for Fe with H removal being an exothermic process for both sites. This exothermic dissociation should be beneficial for hydrogen desorption, but the speed of this reaction at ambient conditions ultimately depends on a favorable activation energy.

Furthermore, we demonstrate for the case of Fe that at least four hydrogen atoms continue to be attracted by the transition metal even when the total hydrogen content of the cluster decreases migrating from the surface sites to the interior sites during the dehydrogenation process, releasing more hydrogen as it diffuses. The relaxed geometries of Fe doped MgH_2 cluster with different hydrogen content are displayed in Figure 3.6.

The observed surface effects of transition metals in our cluster model give support to the gateway (or shuttling) hypothesis of dehydrogenation [37], where transition metals act as catalytic centers for hydrogen atom by continuously attracting new hydrogen atoms from the rest of the cluster as hydrogen desorbs. In addition, we see evidence of iron diffusion upon dehydrogenation, suggesting that iron, and most probably other transition metals, stay in the MgH_2/Mg interface region continuously catalyzing dehydrogenation.

3.4.2 Sodium alanate

At ambient conditions, sodium alanate NaAlH_4 crystallizes in the body-centred tetragonal structure having the $I4_1/a$ space group (see Figure 3.7). In this compound, the Al atom is encapsulated by four hydrogen atoms

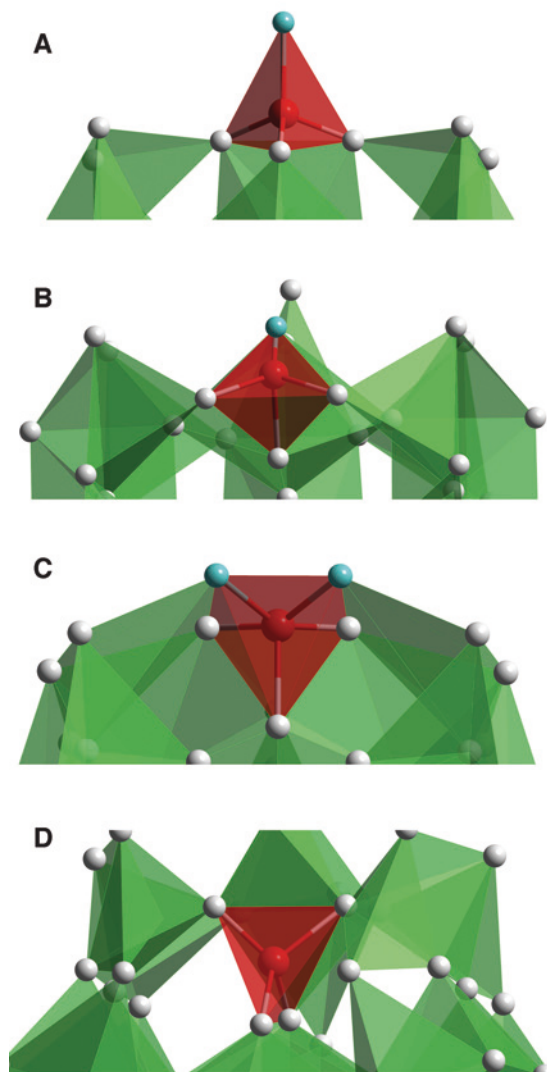


Figure 3.6: Successive dehydrogenation around the Fe atom. At each step, the blue hydrogen atom(s) are removed and the structure reoptimized. A: $\text{Mg}_{30}\text{Fe-H}_{62}$. Fe coordinates four hydrogen atoms in a tetrahedral fashion. B: $\text{Mg}_{30}\text{Fe-H}_{61}$. Tetrahedral coordination reformed after removal and optimization. C: $\text{Mg}_{30}\text{Fe-H}_{60}$. Iron now coordinates five hydrogen atoms. D: $\text{Mg}_{30}\text{Fe-H}_{58}$. Iron becomes tetrahedrally coordinated once again.

forming a tetrahedron in the same way as the C atom is encapsulated by four hydrogen atoms in CH₄. This is also the structure of BH₄[−] complex.

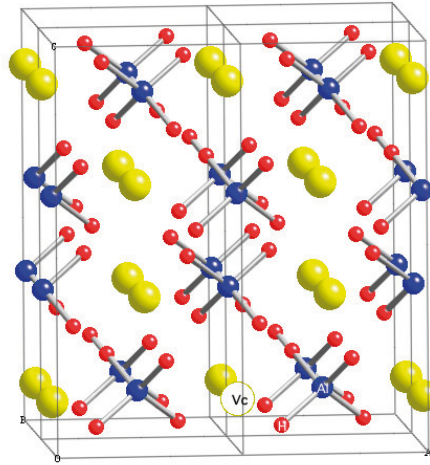
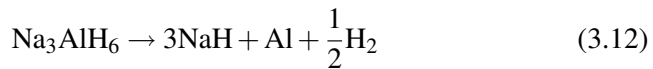
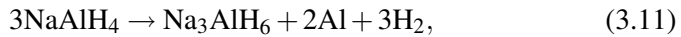


Figure 3.7: The 96-atom supercell geometry of Na₁₆Al₁₆H₆₄. The yellow, blue, and red color atoms correspond to Na, Al, and H respectively.

The dissociation of NaAlH₄ takes place in the following three steps:



and



The first reaction releases 3.7 wt% of hydrogen, while the second one releases 1.9 wt% relative to the starting material, NaAlH₄. The third step requires very high temperature and thus the hydrogen storage capacity of sodium alanate is considered to be 5.6 wt%. Despite this high hydrogen content, the use of NaAlH₄ for applications in on-board hydrogen storage is severely limited by the fact that the chemical reactions above not only display slow kinetics but also they are not reversible. This is due to the strong chemical bonds which hold hydrogen atoms.

The addition of small amount of TiCl₃ was shown not only to significantly improve the kinetics of the reactions in (3.11) and (3.12) but also made those

reactions reversible [38]. This is a breakthrough discovery in the field of solid-state hydrogen storage that has revitalized the researches on complex light metal hydrides and has also highlighted the role of catalysts. This result has motivated a great deal of research with the aim of fully understanding the mechanism of such catalytic effect [39]-[56].

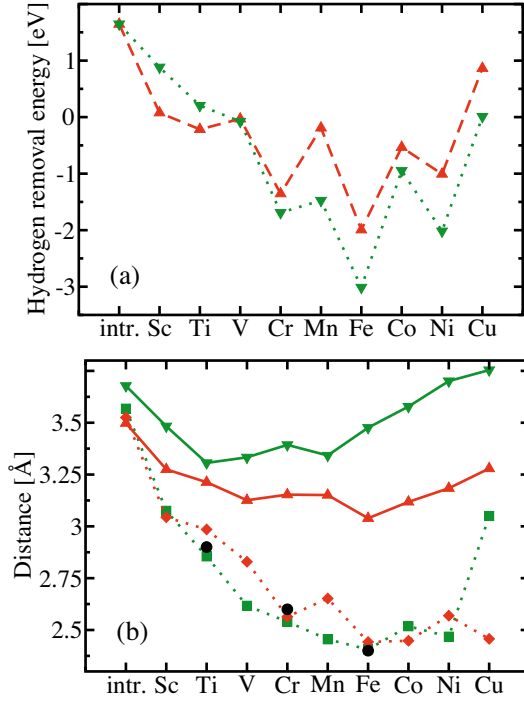


Figure 3.8: (a) Hydrogen removal energy when TM@Al (green dotted) and TM@Na (red dashed). (b) TM-Al distance before removal of hydrogen when TM@Al (green full line) and TM@Na (red full line); TM-Al distance after removal of hydrogen when TM@Al (green dotted) and TM@Na (red dotted); First PDF TM-Al peak from MD simulations (•). ($TM@Na \equiv TM$ replacing Na site).

In order to contribute to this important problem, we have investigated theoretically the effect of Ti doping on the hydrogen bonding in crystalline sodium alanate. The calculations were performed using GGA and PAW method (see Paper II). A 96 atoms supercell was used to model the Ti doping. It was found that as Ti replaces the Na site, the strength of the chemical bond between Al and H is weakened resulting in a lower hydrogen binding energy. This is obtained by calculating the energy needed to remove one hydrogen atom from both the intrinsic and Ti-doped sodium alanate. It was found that it costs 4.0 eV for the former whereas it costs only 1.9 eV for the latter. In these numbers, the internal binding energy of H_2 has not been subtracted meaning that the removal energy is calculated with respect to atomic hydrogen total energy. One contribution to such weakening identified in this study is the change in

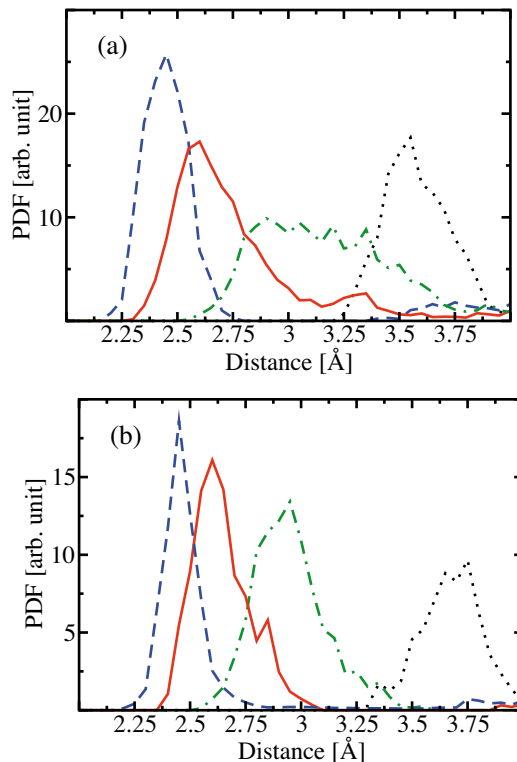


Figure 3.9: Pair distribution function from 400 K *ab initio* molecular dynamics simulations. **(a)** Fe-Al (blue dashed), Cr-Al (red solid) and Ti-Al (green dashed dotted) when TM@Na site and Na-Al (black dotted) in pure NaAlH₄. **(b)** Fe-Al (blue dashed), Cr-Al (red solid) and Ti-Al (green dashed dotted) when TM@Na site and Al-Al (black dotted) in pure NaAlH₄.

the electronic structure, induced by Ti, which has resulted in a lattice relaxation where AlH₄ complex was found to be distorted with some Al-H bonds stretched. However, another important contribution is the formation of Ti-Al bond after the hydrogen atom is removed. This contribution was identified when we compared the results obtained for Ti-doped with those for other 3d-transition metals. This investigation is described in the following.

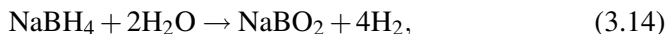
In a further step to improve our understanding on the effect of catalysts in sodium alanate, we have carried out a systematic study on 3d transition metal (TM) substitutional doping on NaAlH₄ by using the same theoretical approach as in the previous work (see Paper III). The calculated hydrogen removal energies for all elements are shown in Figure 3.8 (a). It should be noticed that now these energies are calculated with respect to the total energy of H₂ molecule instead of atomic energy. This means that we account for the gain in energy as H₂ is formed following H removal. This simply leads to a constant shift of the H removal energies, namely by the amount of the H₂ binding energy.

The trend in this curve could not be explained by taking into account only the electronic structure change following the substitution of Na or Al atoms revealing that other effects should be considered. In fact, the lattice relaxation is found to play an important role on the desorption mechanism. Considerable shortening of the TM-Al bond happens regardless whether Na or Al site is occupied by the transition metals. This was first observed in the geometry relaxation of the supercells following the hydrogen removal. As can be observed in Figure 3.8 (b), TM-Al distance follow a similar trend as that for the hydrogen removal energy.

One point that puzzled us was why this strong relaxation could not be observed in the fully hydrogenated supercell. This was solved by employing *ab initio* molecular dynamics simulations at 400 K. The formation of intermetallic bonds between transition metal atoms and Al is demonstrated to be possible as energy barriers can be overcome at finite temperature. The pair distribution function (PDF) for Ti-Al, Fe-Al and Cr-Al are shown in Figures 3.9 (a) and (b). As can be seen, the PDF peaks are situated around the same points regardless the simulation start with TM being at Al or Na sites and this points correspond to the TM-Al distances obtained following the hydrogen removal. These results revealed the strong tendency for forming an intermetallic phase in the doped systems. We believe this is an important contribution to destabilize NaAlH₄, and hence, to improve the kinetics for the hydrogen release. Furthermore, in Cr- and Fe-doped sodium alanate the hydrogen removal energies are lower and the lattice relaxations are bigger when compared to Ti-doped system indicating that the former two elements may display better catalytic properties.

3.4.3 Sodium borate

NaBH₄ slurry has been proposed as an efficient hydrogen storage medium for applications on fuel cell technology [57]-[59]. The hydrogen atoms from both NaBH₄ and H₂O can be released through the following heat-releasing reaction



This reaction is activated by adding a proper catalyst and can be operated at ambient conditions. Furthermore, the by-product NaBO₂ can be recycled into NaBH₄ through a fuel recovery reaction which makes the hydrolysis above a renewable process [60]. The hydrogen gravimetric density in the solution NaBH₄-H₂O is 10.9 wt%, which meets the requirements for on board applications. Actually, sodium borate itself displays also high hydrogen content, namely 10.7 wt%. If this amount of hydrogen could be released in a reversible thermally activated process, the application of NaBH₄ as hydrogen storage material would be significantly broadened. However, this is still not possible. Therefore, it is worthwhile to conduct studies aimed at finding good catalysts to improve the thermodynamics and kinetics properties of its thermal dissociation. An approach that shows promise toward the achievement of this goal is

the addition of impurities that are capable of weakening the B-H bond and of increasing the hydrogen mobility.

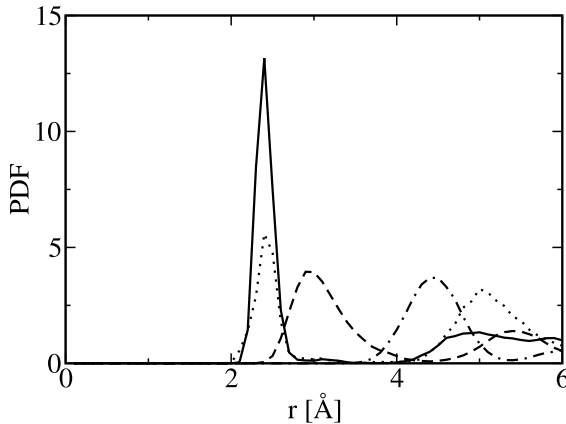


Figure 3.10: Pair distribution function from 400 K *ab initio* molecular dynamics simulations. Solid and dotted lines represent Ti-B pairs when Ti substitute Na (in $\text{TiNa}_7\text{B}_8\text{H}_{32}$ supercell) and B (in $\text{Na}_8\text{TiB}_7\text{H}_{32}$ supercell), respectively. Dashed and dotted-dashed lines represent the Na-B and B-B pairs in the pure NaBH_4 , respectively.

In Paper IV, the supercell approach was employed to investigate Ti as a candidate to catalyze the thermal dissociation of NaBH_4 . The substitution of Ti at Na site is shown to be the most stable configuration when the total energies of isolated atoms are taken as reference energies. In fact, as Ti is substituted in sodium borate lattice, it diminishes the binding energy of nearest neighbor hydrogen atoms regardless of being at Na or B sites. It costs 2.24 eV to remove a hydrogen atom from pristine sodium borate while it costs 1.37 eV when Ti replaces Na, for instance. These energies are calculated by subtracting the energy gain due to H_2 formation. We show that this effect is mainly driven by the formation of Ti-B bond following the hydrogen removal. To further understand this effect, we have performed *ab initio* molecular dynamics simulations at 400 K. The first Ti-B PDF peak is located around 2.3 Å for Ti at both Na and B sites (see Figure 3.10). This is, actually, the calculated distance between Ti and nearest B atoms in the relaxed supercell following the hydrogen removal. It should also be highlighted that Ti-B PDF shows a peak at 2.3 Å for Ti at B site while B-B PDF has the first peak at 4.3 Å showing that Ti migrates in the lattice toward B sites. Therefore, we believe that Ti may combine with B to form an intermetallic phase catalyzing the hydrogen release. Furthermore, we have observed that the mobility of hydrogen near to Ti is higher than that of the corresponding one in the intrinsic systems. Such faster dynamics may help in the hydrogen migration.

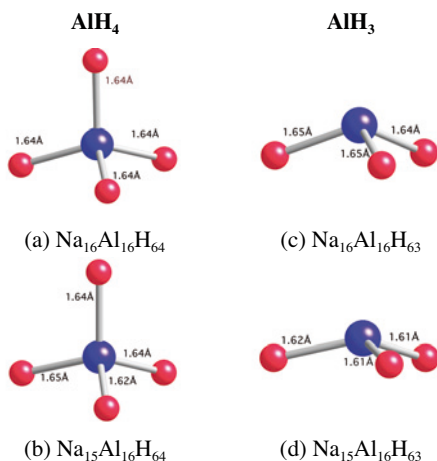
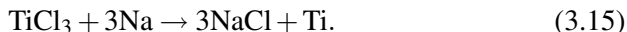


Figure 3.11: The geometries of the AlH_4 complexes in (a) $\text{Na}_{16}\text{Al}_{16}\text{H}_{64}$ and (b) $\text{Na}_{15}\text{Al}_{16}\text{H}_{64}$ supercells and those of AlH_3 complexes in (c) $\text{Na}_{16}\text{Al}_{16}\text{H}_{63}$ and (d) $\text{Na}_{15}\text{Al}_{16}\text{H}_{63}$ supercells. Al and H atoms represented by blue and red balls, respectively.

3.4.4 Vacancy mediated hydrogen desorption

It should be noted that formation of NaCl has also been observed during ball milling of NaAlH_4 with TiCl_3 [61, 62]. This could happen through the following reaction:



Thus, for every TiCl_3 that combines with Na to form NaCl , three Na-vacancies can be created. Even if the Ti atom occupies one of these vacant Na sites, two Na-vacancies will still remain. Furthermore, in these experiments the ball milling technique is employed in order to produce nano-structured compounds. In this kind of experiment, which operates in non-equilibrium thermodynamics conditions, the concentration of metal vacancies may be significantly increased. These are the motivations for us to investigate the effect of Na vacancies on the hydrogen desorption in NaAlH_4 (see Paper V).

The neutral Na vacancy was modeled by using a 96 atoms supercell and the electronic structure was calculated using DFT and PAW method. Very small lattice relaxation and electronic structure change were obtained as Na atom was removed. These results contradicted our first thought, which was the following. The nearest Al atom was supposed to move toward the vacant site and cause the Al-H distances to change. This is because the creation of neutral Na vacancy would deprive the nearest $(\text{AlH}_4)^-$ unit from the extra electron that it needs to be stabilized in the tetrahedral form.

The hydrogen removal energy, on the other hand, was found to be remarkably affected by the Na vacancy. It costs only 0.2 eV to remove a hydrogen

atom from the $\text{Na}_{15}\text{Al}_{16}\text{H}_{64}$ supercell. This process can be exothermic since the two desorbed hydrogen atoms can combine to form a H_2 molecule, and contribute nearly 2.3 eV per H atom of energy into the reaction. However, energy barriers may still need to be overcome. To compare these results with those when Ti atom occupies either a Na or an Al site, one has to remember that the energy needed to remove a hydrogen atom from the $\text{TiNa}_{15}\text{Al}_{16}\text{H}_{64}$ ($\text{Na}_{16}\text{TiAl}_{15}\text{H}_{64}$) supercell is 1.9 eV (2.5 eV) while that from the $\text{Na}_{16}\text{Al}_{16}\text{H}_{64}$ supercell is 4.0 eV, as it was presented in the section 3.4.2. Thus, the hydrogen removal energy in the system containing a Na vacancy is an order of magnitude smaller than that in the perfect crystal.

To understand this result, we show in Figures 3.11 (c) and (d) the geometries of the AlH_3 units following the removal of a H atom from the $\text{Na}_{16}\text{Al}_{16}\text{H}_{64}$ and $\text{Na}_{15}\text{Al}_{16}\text{H}_{64}$ supercells, respectively. Note that while the bonding between Al and H in the AlH_3 unit in the $\text{Na}_{16}\text{Al}_{16}\text{H}_{63}$ supercells remains nearly tetrahedral, that in the $\text{Na}_{15}\text{Al}_{16}\text{H}_{63}$ supercell is very different—namely, it is nearly planar with an Al-H bond length of 1.61-1.62 Å. The stabilization of planar AlH_3 cluster is primarily responsible for the reduced hydrogen removal energy from the $\text{Na}_{15}\text{Al}_{16}\text{H}_{64}$ supercell.

In conclusion, we have shown in this work that the effect of addition of TiCl_3 could have another component, the induction of Na vacancy formation by chemical means, which is much more effective than the interaction of Ti with the sodium alanate lattice itself.

3.5 Mixtures as a new strategy

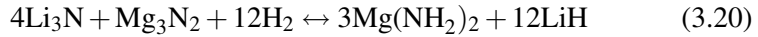
Recently developed hydrogen storage materials use a mixture of chemical hydrides instead of the single phase compounds presented in the previous section. This approach leads to hydrogen sorption reactions with improved thermodynamics, which are so called destabilized reactions. An illustration of this effect is shown in Figure 3.2. One can find many of these mixtures in the literature but, in our studies, we concentrate only in those involving Li, Mg, N and H elements.

Chen *et al.* [63] have shown that it is possible to store up to 11.5 wt% of hydrogen through the following reversible reactions without addition of any catalyst:



As can be observed in Eq. (3.17) the fully hydrogenated state is a mixture of LiNH_2 and LiH . These reactions are reversible, which is an advantage when compared to single phase CLMH like alanates, borates, etc. However, the thermodynamic and kinetic properties still require further improvement before this approach could be considered suitable for on-board applications.

One route to improve them, which has most widely been investigated, consists of partially replacing Li by Mg leading to hydrogen storage in the $\text{Mg}(\text{NH}_2)_2\text{-LiH}$ mixture instead of $\text{LiNH}_2\text{-LiH}$ mixture. This has been achieved independently by four research groups, using different starting materials. Both Luo [64] and Xiong et al. [65] investigated the H-release from the $2\text{LiNH}_2\text{-MgH}_2$ mixture, Leng et al. [66] studied the H-release from $3\text{Mg}(\text{NH}_2)_2\text{-8LiH}$ mixture, and finally Nakamori et al. [67] followed a different approach, studying the hydrogenation of the $\text{Mg}_3\text{N}_2\text{-4Li}_3\text{N}$ mixture. The common outcome of all these experiments was a fully hydrogenated state composed of a mixture of LiH and $\text{Mg}(\text{NH}_2)_2$ but with different composition ratios. The following reversible hydrogen storage reactions have been identified:



These modified systems display better thermodynamics than those from Eqs. (3.16) and (3.17). Moreover, their theoretical hydrogen capacity is quite high, namely 5.6 wt% for Eq. (3.18), 6.9 wt% for Eq.(3.19), and 9.1 wt% for Eq. (3.20). These experimental findings have made Li-Mg-N-H systems one of the most promising hydrogen storages media. However, the fundamental understanding of the mechanisms and thermodynamics of the reactions at work is still missing. The main challenge is the determination of the crystal structure of new hydride phases.

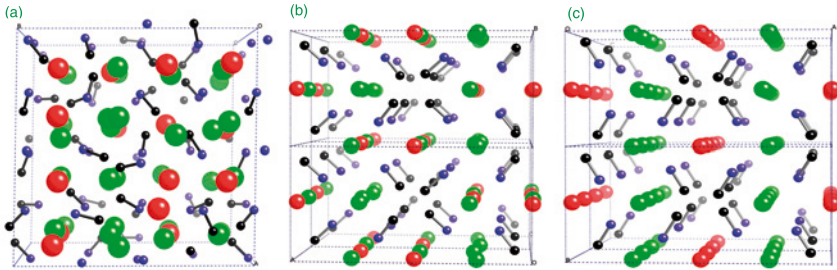


Figure 3.12: Structures of $\text{Li}_{32}\text{Mg}_{16}(\text{NH})_{32}$ obtained from (a) *ab initio* molecular dynamics simulated annealing calculations and geometry optimization of (b) mixing and (c) segregation configurations. The green, red, blue and black spheres represent Li, Mg, N and H atoms, respectively

We have studied several possible conformations for the crystal structure of $\text{Li}_2\text{Mg}(\text{NH})_2$ and we confirm the orthorhombic structure belonging to space group *Iba*2, the so-called α -phase, as the ground-state configuration (see Paper VII). This structure has recently been resolved from both x-ray and neu-

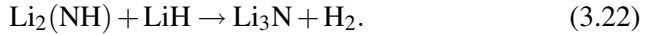
tron diffraction data [68]. In this compound Li^+ and Mg^{2+} mix up in the cation sub-lattice, which is consistent with the fact that these two cations display similar ionic radii, viz., in units of Ångström, 0.59 (0.57), 0.76 (0.72) and 0.92 (0.89) for Li^+ (Mg^{2+}) with coordinations IV, VI and VIII, respectively. This close similarity in ionic radii would not be expected for any arbitrary pair of cations, and it is thus unique for the combination Li-Mg. Another important feature is the orientation of the NH units, with H atoms pointing toward the cation vacant sites in order to minimize electrostatic interaction between positively charged hydrogen atoms and cations (Li and Mg).

The replacement of every two Li atoms by one Mg when going from lithium imide to this mixed imide system lead to higher hydrogen binding energy. It costs 2.45 eV to remove a hydrogen atom from $\text{Li}_2\text{Mg}(\text{NH})_2$, whereas it costs 2.42 eV from Li_2NH , showing that the N-H bond is slightly stronger in the former. In this calculation, we have used the orthorhombic structure (space group $Pnma$) for lithium imide.

To compare the thermodynamics of hydrogen release reaction from the mixture of $\text{Li}_2\text{Mg}(\text{NH})_2$ and LiH , and the mixture of Li_2NH and LiH , we have evaluated the zero-temperature enthalpy of the following reactions:



and



We have found both reactions above to be endothermic with an enthalpy of $84.1 \text{ kJ (mol H}_2\text{)}^{-1}$ and $118 \text{ KJ (mol H}_2\text{)}^{-1}$, respectively. Since the reaction entropies for this kind of reaction is highly dominated by the hydrogen gas entropy, the temperature that makes the reaction in Eq. (3.21) thermodynamically favorable ($\Delta H = T\Delta S$) may be lower than that for the reaction in Eq. (3.22).

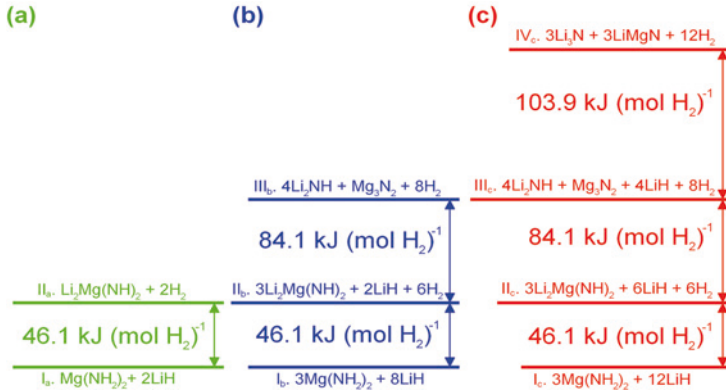


Figure 3.13: Enthalpy diagrams for the corresponding reactions in (a) Eq. (3.18), (b) Eq. (3.19), and (c) Eq. (3.20).

In Paper VIII, we provide a systematic investigation of the thermodynamics of the reactions in Eq. (3.18) - (3.20). The enthalpy is calculated by the sum of the electronic total energy and zero point vibration energy. The vibrational free energies that appear at finite temperatures are expected to constitute only a small contribution to the reaction enthalpy, which will not change the conclusions concerning the trends in the thermodynamics of these reactions. Part of the results are summarized in Figure 3.13. In this work, we show that the mixture of $\text{Mg}(\text{NH}_2)_2$ and LiH is energetically more stable than that of LiNH_2 and MgH_2 , illustrating that the stabilization of the hydrogenated state containing $\text{Mg}(\text{NH}_2)_2$ and lithium hydride is driven by equilibrium thermodynamic conditions rather than reaction barriers.

We have investigated the thermodynamics of the hydrogen sorption reactions for the three different $\text{LiH}/\text{Mg}(\text{NH}_2)_2$ composition ratios obtained in Eq. (3.18)-(3.20), viz. 2/1, 8/3 and 12/3. For all these ratios, the hydrogen release is initiated by the same reaction with an enthalpy of $46.1 \text{ kJ (mol of H}_2\text{)}^{-1}$. This initial release is followed by a second desorption step for mixing ratios 8/3 and 12/3 with a larger reaction enthalpy of $84.1 \text{ kJ (mol of H}_2\text{)}^{-1}$, and for the mixing ratio 12/3 by a third step with an even larger reaction enthalpy of $103.9 \text{ kJ (mol of H}_2\text{)}^{-1}$. Thus, while the weight percentage of hydrogen stored in the respective reactions with various mixing ratios differs, the actual amount of hydrogen gas released at the lowest (and presumably, the only practical) temperature remains the same. Higher temperatures are required to desorb all the hydrogen stored in the system, which renders it virtually inaccessible at conditions suitable for vehicular hydrogen storage applications. Furthermore, the most stable dehydrogenated state for the mixing ratio 12/3 is not the one shown in Eq. (3.20), but rather Li_3N is mixed with Mg_3N_2 forming LiMgN . The corresponding mixing enthalpy is found to be $56.1 \text{ kJ (mol of Mg}_3\text{N}_2\text{)}^{-1}$.

The replacement of LiH by MgH_2 as reaction partner of $\text{Mg}(\text{NH}_2)_2$ in the fully hydrogenated state was also investigated. The hydrogen gravimetric density of this mixture is 7.4 wt%. The reaction enthalpy was found to be $11.5 \text{ (mol of H}_2\text{)}^{-1}$ implying that this mixture is not stable at ambient conditions. Nevertheless, it might still be possible to raise operation temperature for such reaction by applying higher pressure to the system.

4. Hydrogen storage II: Physisorption

To understand the mechanism of non-dissociative H_2 adsorption on high surface area materials is of great importance to the development of efficient hydrogen storage tanks displaying fast kinetics for the loading-releasing processes. In this chapter, the results of our studies on hydrogen storage in metal-organic frameworks, which is a compound that shows great promise in that respect, are summarized. In the next section, the general background information is introduced. The results are in sections 4.2 and 4.3.

4.1 Introduction

As already described in the previous chapter, H_2 molecules approaching the material surface can be non-dissociatively adsorbed on a shallow potential well (physisorption). In Figure 4.1, we display a qualitative illustration of the Lennard-Jones potential energy curve for hydrogen binding to a metal similar to that one presented in Figure 3.1, with the only difference being the presence now of an energy barrier for the molecular-atomic transition. It should be noted that the energy curves of the molecular and atomic states cross each other at an energy value that is higher than that of H_2 in the gas phase forming in this way an energy barrier for the molecular dissociation. This barrier raises the statistical probability of having the molecules populating the physisorption states. Thus, to tune the properties of those hydrogen storage systems which make use of the physisorption mechanism, one has to look for ways to adapt the height of such an energy barrier for the molecular-atomic transition and also the depth of the physisorption well, i.e. the strength of the adsorption interaction.

Carbon based materials (nanotubes, fullerenes, porous materials, etc) [5], metal organic frameworks (MOFs) [7], molecular clathrates [6] among others are able of adsorbing a significant amount of hydrogen in a non-dissociative manner due to their high surface area. In these systems, the hydrogen sorption processes display good reversibility and fast kinetics. However, the weak dispersive interactions that hold H_2 molecules (resulting in a shallow physisorption well) require cryogenic temperatures and/or high pressures in order to guarantee a significant storage capacity. These thermodynamic conditions do not meet the requirements for on board application. Therefore, the main goal here is to devise ways to strengthening the hydrogen adsorption interactions without causing the molecular dissociation. This is exactly the contrary of what the research on chemical hydrides must achieve. It is well accepted that

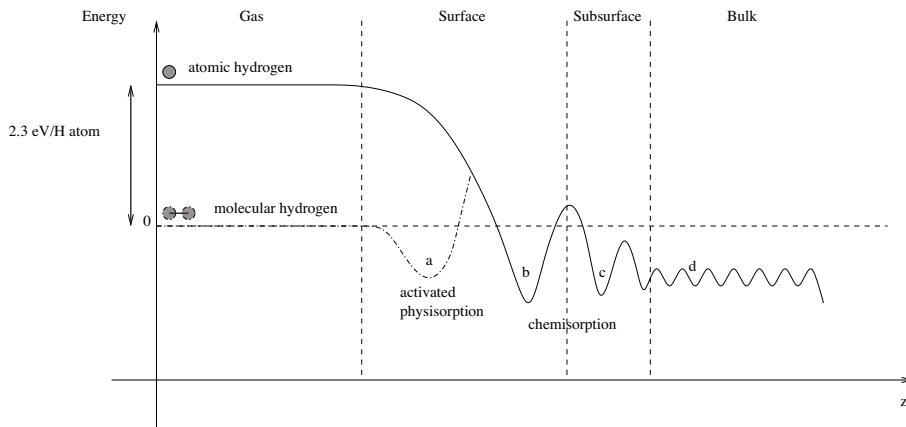


Figure 4.1: Qualitative illustration of the Lennard-Jones potential energy curve for hydrogen (in the atomic and molecular states) interacting with a metal where four different events are illustrated, namely (a) activated physisorption, (b) surface chemisorption (c) sub-surface chemisorption and (d) bulk chemisorption/diffusion. The potential energy curve for the molecular hydrogen is drawn only until it meets the potential energy curve for the atomic hydrogen. Adapted from Ref. [30].

to significantly enhance the H_2 affinity in these materials, the binding mechanism should include other contributions such as electrostatic and/or orbital interactions rather than being purely dispersive like [69].

In the current literature, one can find many prospective approaches to enhance the non-dissociative H_2 -interaction with host materials, which mainly used the coating the adsorbate surfaces with transition metals. For instance, Yildirim and Ciraci [70] have shown that titanium decorated carbon nanotubes can strongly adsorb up to 8 wt% of hydrogen. Zhao *et al.* [71] have found that transition metal coated C_{60} molecules could act as good hydrogen adsorbents working at room conditions. More recently, Lee *et al.* [72] have performed a combinatorial search for nanostructured hydrogen storage materials where Ti-decorated *cis*-polyacetylene was found to be an optimal material. The strong hydrogen binding affinities were mainly attributed to the orbital interactions between hydrogen σ bond and transition metals d states. The main problem here is that the fabrication of these systems is still a challenge primarily due to the tendency of the coating atoms to form clusters [73]. An alternative approach for strong non-dissociative H_2 binding comes also from the possibility of adsorbing hydrogen molecules on light non-transition metal ions, e.g. Li^+ , Na^+ , Mg^{2+} and Al^{3+} [69, 74]. These bare metal ions can cluster many H_2 molecules around themselves with quite strong binding energy ranging from 12–340 kJ mol^{-1} . For the alkali metals (Li^+ and Mg^{2+}) H_2 is bound through electrostatic charge–quadrupole and charge–induced dipole interactions. For Al^{3+} and Mg^{2+} , which display the highest binding energies, there are other contributions coming from the orbital interactions. Despite such good binding affinity, these bare metal ions are difficult to realize in real systems. They

usually form complexes in which only part of the charges are available for the interaction with the hydrogen molecules.

In this thesis, we have focused on improving the hydrogen storage properties of metal-organic frameworks. In the next two sections, our studies on the hydrogen storage in metal-organic frameworks are described.

4.2 H₂ adsorption in metal-organic frameworks

We have investigated in particular the Metal-organic framework-5, which is made up from 1,4-benzenedicarboxylate O₂C-C₆H₄-CO₂ (BDC) linkers joining together Zn₄O clusters to form a cubic periodic framework, which has the formula unit (f.u.) Zn₄O(O₂C-C₆H₄-CO₂)₃. The structure of MOF-5 is displayed in Figure 4.2. This framework has been shown to reach a H₂-uptake

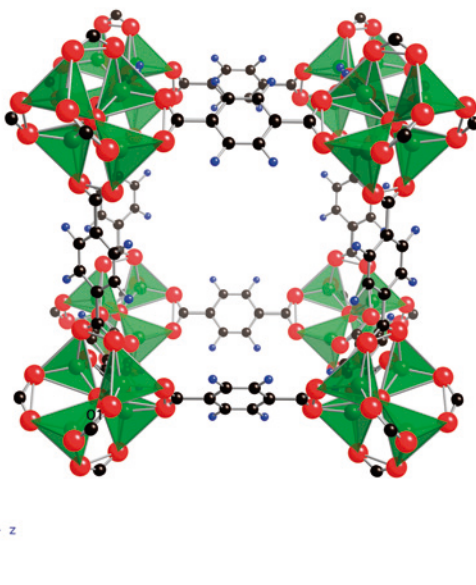


Figure 4.2: The structure of Metal-Organic Framework-5 (MOF-5). O, C and H atoms represented by red, black and blue balls, respectively. Zn atoms represented by the balls located in the center of the green tetrahedra.

of only 1.3 wt% at 78 K and 1 bar [75]. This thermodynamical condition and also this storage capacity does not meet the requirements that have been set up for on-board applications. Any improvement of such properties requires the understanding of how and where H₂ molecules are adsorbed on the pore wall, which is a heterogeneous surface.

Table 4.1: Binding energies of H_2 in Zn-MOF and Cd-MOF at cup site, MO_2 and MO_3 sites with $M \equiv Zn$ and Cd. "Cup-perpendicular" and "cup-parallel" respectively refer to the H_2 molecular orientation which is perpendicular and parallel along the three-fold rotation axis for cup site.

EXC functional	H_2 binding site	ΔE_b (meV)		
		Zn-MOF	Cd-MOF	Zn-MOF
LDA	cup-parallel	-125.6	-133.3	-133 ^a
	cup-perpendicular	-157.7	-160.4	-160 ^a
	MO_2	-86.5	-125.2	-108 ^a
	MO_3	-110.2	-149.7	-115 ^a
GGA (PW91)	cup-parallel	-18.9	-22.3	-
	cup-perpendicular	-32.8	-37.0	-
	MO_2	-32.7	-29.2	-
	MO_3	-21.0	-31.8	-
GGA (PBE)	cup-parallel	-8.4	-7.2	-9.5 ^b
	cup-perpendicular	-17.3	-21.3	-17.9 ^b
	MO_2	-8.3	-9.6	-7.5 ^b
	MO_3	-6.4	-17.9	-12.5 ^b

^a results from [76]

^b results from [77]

Yildirim *et al.* [76] have shown from neutron diffraction data and first principles calculations that the first preferable adsorption sites are at the center of the three ZnO_3 triangular faces (see Figures 4.3 (a) and (b)), which were termed "cup sites". The next populated sites are on top of single ZnO_3 triangles (denoted " ZnO_3 sites"), just above the two oxygen ions (denoted " ZnO_2 sites") and on the top of the hexagonal linkers (denoted "hex site"). These former two sites are illustrated in Figures 4.3 (c) and (d). Other theoretical studies by Mueller *et al.* [77] and Samanta *et al.* [78] have also confirmed that most of the adsorption sites are situated near the Zn_4O clusters. However, the strength of the physisorption is highly dependent on the exchange-correlation functionals used in those calculations with LDA and GGA giving rise to overbinding and underbinding, respectively. None of these functionals are in fact appropriate to describe dispersive (van der Waals) interactions. However, to model MOF-5 by investigating only small pieces, which allows calculations with more suitable methods, is believed to produce misleading results [77]. There is actually a compromise one needs to make between using the best theoretical approach and modeling the full periodic structure of MOF-5. Therefore, the theoretical investigation of this system is a challenging task.

In Paper IX, we have performed a comparative theoretical investigation between two distinct MOF-5 composed of Zn_4O and Cd_4O clusters. The hydro-

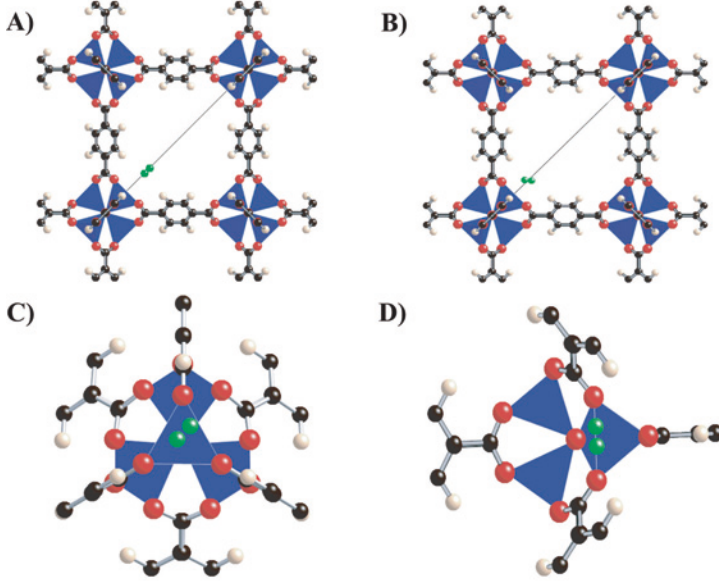


Figure 4.3: The MOF-5 adsorption sites. Adsorbed hydrogen molecule on *Cup* site with orientation (A) parallel and (B) perpendicular to the three-fold rotation axis (solid line). (C) MO_3 site with adsorbed hydrogen perpendicular to the three-fold rotation axis and (D) MO_2 site with H_2 molecule perpendicular to the two-fold rotation axis ($M \equiv Zn, Cd$). Color scheme as follows: Zn (blue), O (red), C (black), framework H (white) and adsorbed H (green).

gen binding energies were calculated through the following expression

$$E_b = E_T(M - MOF : H_2) - [E_T(M - MOF) + E_T(H_2)], \quad (4.1)$$

where $E_T(M - MOF : H_2)$, $E_T(M - MOF)$ and $E_T(H_2)$ are the total energies of the MOF-5 unit cell containing the H_2 molecule, the pure MOF-5 unit cell and the free H_2 molecule in the gas phase, respectively. M-MOF means either Zn-MOF or Cd-MOF. We have employed in this investigation three different functionals, namely LDA, PBE and PW91. For the cup site, we have considered two orientations of the H_2 molecules whereas for MO_2 and MO_3 sites, we have investigated only the side-on configuration. The results are presented in Table (4.1). One can observe that the binding energies are indeed highly dependent on the exchange-correlation functionals. Since we are dealing with dispersive interaction, with binding energies typically in the range 50 - 80 meV [69], the LDA is found to produce over-binding results. Among PW91 and PBE it is difficult to judge which one provides the most accurate description. For that, one would need to make comparison with experimental results but such numbers are hard to obtain. Despite such discrepancy for the binding energy values, all functionals provide the same trend for the strength of the binding sites, with the following hierarchy: $E_b^{cup} > E_b^{MO_3} > E_b^{MO_2}$ with $M \equiv$

Zn, Cd, except for the GGA results for Zn-MOFs where $E_b^{ZnO_3} < E_b^{ZnO_2}$. The trend obtained with LDA is in good agreement with the populations obtained from neutron diffraction [76] in Zn-MOF-5 where *Cup* and *ZnO₃* sites are populated first followed by *ZnO₂* site. We have also obtained good agreement with previous theoretical works on Zn-MOF-5 as can be observed from the numbers in the last column of Table (4.1).

It should also be noted that the binding energies of Cd-MOF are systematically higher than those of Zn-MOF. However, this rise in energy is not enough to significantly rise the operation temperatures of the hydrogen storage process. It has been shown that to store H₂ molecules at 1bar and in the temperature interval 0 - 50 °C the hydrogen adsorption energies must lie in the range 350 - 440 meV [69]. This is achievable only if other contributions to the hydrogen-surface interaction is included on top of the van der Waals forces. In the next section, we present our studies directed to achieving this goal.

4.3 Functionalized metal-organic frameworks

To improve hydrogen sorption in MOFs, the following routes are being pursued: topological engineering of the pore shape [7], the insertion of other adsorbate surfaces inside the pores [79], the synthesis of light-metal MOFs [80, 81], and the entanglement of frameworks (framework catenation) [82, 83]. In order to achieve stronger H₂-surface interactions, which is the more challenging problem, most of the studies have turned to investigate the introduction of electron-donating ligands to the organic linkers and also to the synthesis of so-called open metal sites [84].

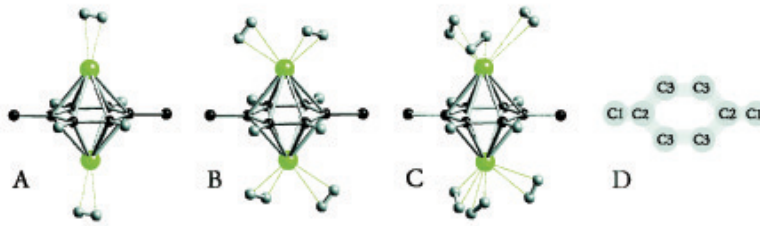


Figure 4.4: Optimized geometries of adsorbed hydrogen molecules on BDC:2Li in the framework of MOF-5 with (A) 1 H₂ per Li, (B) 2 H₂ per Li, and (C) 3 H₂ per Li. Color scheme as follows: C (black), Li (Green), and H (Grey). The rest of the framework have been omitted for clarity. In (D) a schematic picture of the C atoms in the BDC unit is shown.

We have studied the effect of coating MOF-5 with Li atoms on hydrogen adsorption properties (see Paper X). The idea is to let Li atoms be adsorbed on the organic linkers (BDC) in order to create the desired ionic state Li⁺, which is beneficial to rise the hydrogen adsorption energy as discussed in the introduction of this chapter. In fact, it was found that each BDC is able of

binding two Li atoms carrying a charge of $+0.9e/\text{Li}$. In this framework, the organic linkers are isolated from each other and consequently, so are the Li atoms. This is an important feature which guarantees that the entire on-site Li charge will be available to interact with hydrogen molecules. To investigate

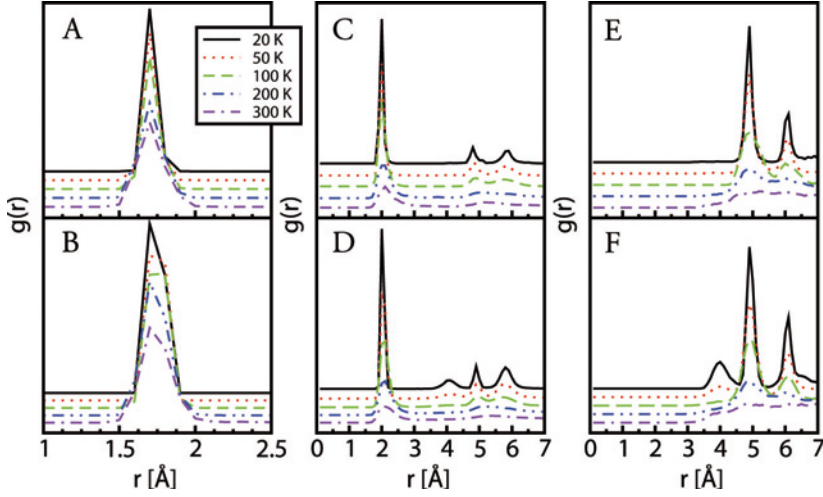


Figure 4.5: Pair distribution functions from *ab initio* molecular dynamics simulations. PDF of $\text{C}_6^{\text{CoM}}\text{-Li}$ pairs with (A) 5 H_2 per formula unit and (B) 18 H_2 per formula unit. PDF of $\text{Li-H}_2^{\text{CoM}}$ pairs with (C) 5 H_2 per formula unit and (D) 18 H_2 per formula unit. PDF of $\text{Zn-H}_2^{\text{CoM}}$ pairs with (E) 5 H_2 per formula unit and (F) 18 H_2 per formula unit.

the tendency of Li atoms to form clusters, we have also optimized the structure containing a Li_{12} cluster inside the pore. The calculated total energy of this structure is found to be 0.25 eV/Li higher than that containing Li adsorbed on the BDC rings showing that clustering is energetically not favored.

The geometries with 2 H_2 , 4 H_2 and 6 H_2 molecules adsorbed on 2Li-BDC complexes are displayed in Fig 4.4. The adsorption energies were calculated as

$$\Delta E_b^{\text{H}_2}(n) = E_T(\text{MOF} : \text{Li}^a : n\text{H}_2^a) - E_T(\text{MOF} : \text{Li}^a) - nE_T(\text{H}_2) \quad (4.2)$$

where $E_T(\text{MOF} : \text{Li}^a : n\text{H}_2^a)$, $E_T(\text{MOF} : \text{Li}^a)$, and $E_T(\text{H}_2)$ are the total energies of MOF-5 containing the adsorbed $\text{Li-}n\text{H}_2$ clusters, of MOF-5 containing the adsorbed Li atoms, and of H_2 in the gas phase, respectively. We have found binding energies of $18 \text{ kJ (mol H}_2)^{-1}$ for $n=1$, $16 \text{ kJ (mol H}_2)^{-1}$ for $n=2$, and $12 \text{ kJ (mol H}_2)^{-1}$ for $n=3$. The latter is more than two times larger than that for H_2 adsorption on pure BDC, which is about $5 \text{ kJ (mol H}_2)^{-1}$ [85]. This is mainly due to the charge-quadrupole and charge-induced dipole interaction between Li^+ and H_2 molecules.

Furthermore, we show from *ab initio* molecular dynamics simulations, with a hydrogen loading of 18 H₂ per formula unit, that a hydrogen uptake of 2.9 wt% at 200 K and 2.0 wt% at 300 K is achievable. This is concluded from the analysis of the pair distribution functions (PDF) for the Li-H₂^{CoM} pairs with H₂^{CoM} representing the H₂ center of mass (see Figures 4.5 (c)-(f)). In order to show that the Li-nH₂ complexes stay attached to the framework, we display in Figures 4.5 (a) and (b) the PDF for the C₆^{CoM}-Li pairs with C₆^{CoM} representing the center of mass of C₆ organic rings. It should be pointed out that with those hydrogen uptake at 200 K and 300 K, Li decorated MOF-5 would display the highest hydrogen storage capacity among the metal-organic frameworks.

In conclusion, we have shown in this work a route to achieving stronger hydrogen adsorption interactions by coating the pore walls with Li atoms, an approach already investigated for carbon nanotubes and C₆₀ molecules. However, with the advantages that MOFs can be fabricated at lower costs and using simpler technologies and also that in MOF-5 the adsorption sites for the coating atoms are well separated from each other what guarantees that the entire on-site Li charge will be available to interact with hydrogen molecules. One next step would be the investigation of the effect of coating MOFs with other chemical elements like 3d transition metals. In this case, the interaction between 3d orbitals and hydrogen σ bond could rise even further the H₂ binding energy. However, our preliminary results for Sc and Ti showed that metal clustering in the center of the pore is energetically favored. It should also be pointed out that other research groups have also reached the conclusion that Li doped MOFs significantly enhance the hydrogen gas uptake based on both theoretical [86] and experimental [87] results showing that this is indeed a promising approach to improve the properties of this metal-organic frameworks for applications as hydrogen storage medium.

5. Structural phase transition

The chemical hydrides undergo several structural transformations induced by pressure and/or temperature. The understanding of the underlying physics of these phenomena is important from fundamental and applied viewpoints. In this chapter, the summaries of the results of our studies on this topic are presented. The presentation is divided into two parts. In the first, the results on the pressure-induced phase transition in NaBH_4 and ErH_3 are presented. In the second, results on the temperature-induced order-disorder phase transition in Li_2NH are presented.

5.1 Pressure-induced structural transformation

5.1.1 Thermodynamics

The most stable structure at a given pressure and temperature is the one that minimizes the Gibbs free energy, $G(T, P) = H(T, P) - TS(T, P)$. We have assumed here that finite temperature effects, such as the changes in the vibrational free energies and also the changes in the configurational entropies (small for perfect crystalline solids), as the system undergoes the phase transition, can be neglected without compromising the main conclusions. Therefore, we have searched for the new structural phases calculating basically the enthalpy at 0K, which is given by

$$H(V) = E(V) + PV, \quad (5.1)$$

where $E(V)$ is the electronic total energy, V is the volume of the unit cell and P is the external pressure. As can be observed, we neglect also the zero point energy. However, It is important to highlight that here PV is not negligible because we are dealing with very high pressures. In practice, we calculate the total energy for different volumes of cell (usually internal coordinates and cell shape are allowed to relax) producing a set of energy (E) - volume (V) values, which are fitted to an equation of states (EOS). Then, from the first derivative of this equation with respect to volume, we obtain the $P(V)$ relation and so the enthalpy $H(V)$. The most commonly used EOS for solid is the Murnaghan equation of state [88], which is written as

$$E(V) = E_0 + \frac{B_0 V}{B'_0} \left(\frac{(V_0/V)^{B'_0}}{B'_0 - 1} + 1 \right) - \frac{B_0 V_0}{B'_0 - 1}, \quad (5.2)$$

with V_0 being the equilibrium volume, B_0 the bulk modulus at equilibrium volume and B'_0 the partial derivative of bulk modulus with respect to pressure at constant temperature calculated at equilibrium volume. E_0 , in (5.2), is the total energy calculated at V_0 .

Francis Birch [89] generalized the Murnaghan EOS which leads to the so-called third-order Birch-Murnaghan equation of state where the pressure is given by:

$$P(V) = \frac{3B_0}{2} \left[\left(\frac{V_0}{V} \right)^{\frac{7}{3}} - \left(\frac{V_0}{V} \right)^{\frac{5}{3}} \right] \times \left\{ 1 + \frac{3}{4} (B'_0 - 4) \left[\left(\frac{V_0}{V} \right)^{\frac{2}{3}} - 1 \right] \right\} \quad (5.3)$$

and the total energy is found by integrating the pressure yielding

$$E(V) = E_0 + \frac{9V_0B_0}{16} \left\{ \left[\left(\frac{V_0}{V} \right)^{\frac{2}{3}} - 1 \right]^3 B'_0 + \left[\left(\frac{V_0}{V} \right)^{\frac{2}{3}} - 1 \right]^2 \left[6 - 4 \left(\frac{V_0}{V} \right)^{\frac{2}{3}} \right] \right\} \quad (5.4)$$

The Birch-Murnaghan equation of state is usually more appropriate than Murnaghan equation of states to describe high pressure data. We have found very small difference between these two EOS for the systems investigated in this thesis.

5.1.2 NaBH₄

In Paper XI, we present a combined experimental and theoretical study of NaBH₄ under high pressure. From the Raman spectroscopic data, it was found that NaBH₄ undergoes a pressure induced phase transition from its fcc structure (α -NaBH₄) to a new high pressure phase (β -NaBH₄). The transformation starts above 10 GPa with the pure high pressure phase being established above 15 GPa, and it is shown to be reversible with respect to pressure release. A transition back to the α -phase occurs at the somewhat lower pressures of 8-11 GPa.

From the analysis of the Raman spectra, the new high pressure phase is expected to be either orthorhombic or monoclinic, with the BH₄ cluster displaying lower symmetry. Through a cooling experiment, it was also shown that the new high pressure phase does not correspond to the low temperature tetragonal (P-421c) phase. We have studied theoretically six closely related potential structures, namely tetragonal-P-421c (low temperature phase), α -NaBH₄ (cubic-F43m), α -LiAlH₄ (monoclinic, P21/c), α -NaAlH₄ (tetragonal-I41/a), KGaH₄ (orthorhombic-Cmc21), α -LiBH₄ (orthorhombic-Pnma). The new high pressure phase was found to show α -LiAlH₄ type structure. The calculated transition pressure of 19 GPa agrees quite well with the experimental finding of 15 GPa. Furthermore, a slight distortion observed in the BH₄ supports the lower symmetry expected for this cluster. A subsequent transformation occurs from the β -NaBH₄ to α -LiBH₄ type structure (γ -phase) at 33 GPa. The differences in enthalpy for LiAlH₄, LiBH₄ and NaAlH₄ type struc-

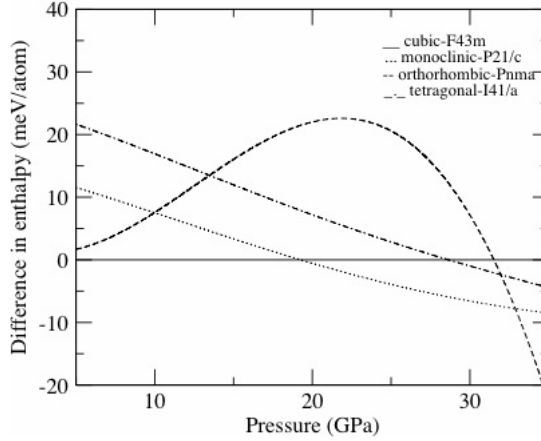


Figure 5.1: The difference in enthalpy for LiAlH_4 , LiBH_4 and NaAlH_4 type structures with reference to $\alpha\text{-NaBH}_4$ as a function of pressure.

tures with reference to $\alpha\text{-NaBH}_4$ as a function of pressure are displayed in Figure 5.1. In addition, we also discuss the electronic structure of both α - and β - NaBH_4 . The main change corresponds to the band gap narrowing in the β -phase, which is due to the broadening of Na antibonding states in the conduction band.

5.1.3 ErH_3

In the fully hydrogenated state, the yttrium and most of rare-earth metals are shown to form a trihydride compound with HoD_3 -type structure, which belongs to the space group $\text{P}3\text{cl}(\text{D}_{3d}^4)$. This structure is viewed as a hexagonal close-packed (hcp) structure with hydrogen atoms slightly distorted away from the usual octahedral and tetrahedral sites. Under high pressure it is expected to undergo structural phase transitions [90, 91]. First-principles calculations have predicted that YH_3 transforms from HoD_3 -type to cubic structure at 1.5 GPa [91], which is accompanied by an insulator-metal transition. The cubic phase was first observed in the fully hydrogenated Y-Mg alloys in which the fcc YH_3 coexists with $\gamma\text{-MgH}_2$. Since the cubic phase was predicted the existence of the cubic phase and also the metal-insulator transition has been questioned. Wijngaarden *et al.* [92] using high-pressure diamond anvil cell and optical measurements have obtained neither the metallic state nor the cubic phase in YH_3 up to 25 GPa. They have predicted that the insulator-metal transition might occur above 55 ± 8 GPa. The cubic phase was achieved more recently by Ohmura *et al.* [93]. Almeida *et al.* [94] have extended the theoretical investigation by employing GW calculations which was able to prove that this high pressure phase indeed display metallic behavior. In this investigation they have found a transition pressure of 20 GPa. This new value is attributed to the atomic relaxation effects that were not included in the first work. On

top of that they have also shown that this phase is dynamically stable in the studied pressure interval.

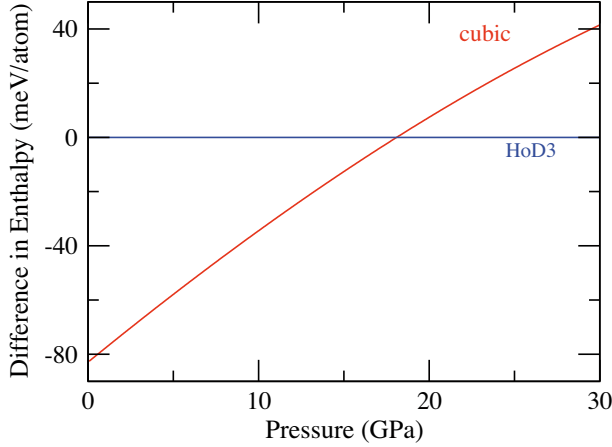


Figure 5.2: The difference in Enthalpy between the HoD₃ and cubic phases as a function of pressure.

Palasyuk *et al.* [95] discovered that ErH₃ undergoes a similar pressure-induced phase transformation from HoD₃ to a cubic phase at 15 GPa. They have also mentioned in their paper that such a transition has also been observed by a research group from Sandia National Laboratory in USA. Motivated by these experimental findings, we have used first-principles theory to investigate such structural phase transformation (see Paper XII). In these calculations, we have used GGA-PW91 functional and PAW method. The cubic structure is modeled with the Er atoms occupying the fcc lattice and hydrogen atoms distributed into the octahedral and tetrahedral sites. The calculated difference in enthalpy between the HoD₃ and cubic phases, with the convention $\Delta H = H_{\text{HoD}_3} - H_{\text{cubic}}$, is displayed in Figure 5.2. As can be seen the HoD₃ phase is stable at ambient pressure and at 17 GPa it shows a transition to the cubic phase. This transition pressure is in good agreement with the experimental value of 15 GPa [95]. The volume collapse at the transition was determined to be 7.7%, which compares quite well with the experimental finding. The calculated equilibrium volume for HoD₃ phase differs by only 0.8% from the experimental value whereas for the high pressure cubic phase the discrepancy between the calculation and experiment is about 7.9%. Furthermore, from the analysis of the electronic density of states, we have found that this structural transition is accompanied by an insulator-metal transition as in YH₃. Additionally, we also predict a similar phase transition in the GdH₃ at 11 GPa.

5.2 Temperature-induced structural phase transition in lithium imide

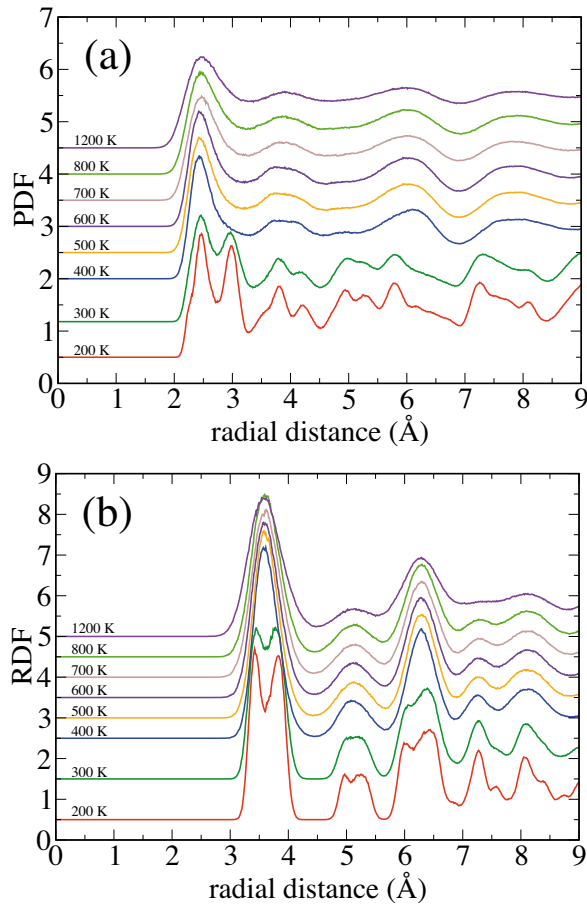


Figure 5.3: (a) Li-Li and (b) N-N pair distribution functions in the temperature range 200–1200 K.

As can be observed in Eqs. (3.16) and (3.17), lithium imide (Li_2NH) is an intermediate state of an important hydrogen storage reaction. Since this result was published [63], Li_2NH has attracted considerable attention from both experimental and theoretical research groups [96]–[101]. This compound is expected to undergo a temperature-induced structural phase transition at around 400 K, which is believed to be of the order-disorder type of transition [101]. This kind of transition is difficult to study through x-ray diffraction measurement due to the low x-ray scattering cross sections of Li and H, which are the elements concerned in this transition. In fact, to understand the underlying physics of this transformation, it is necessary to perform theoretical investiga-

tions to complement the experimental efforts. In this case, *ab initio* molecular dynamics simulations can play an important role.

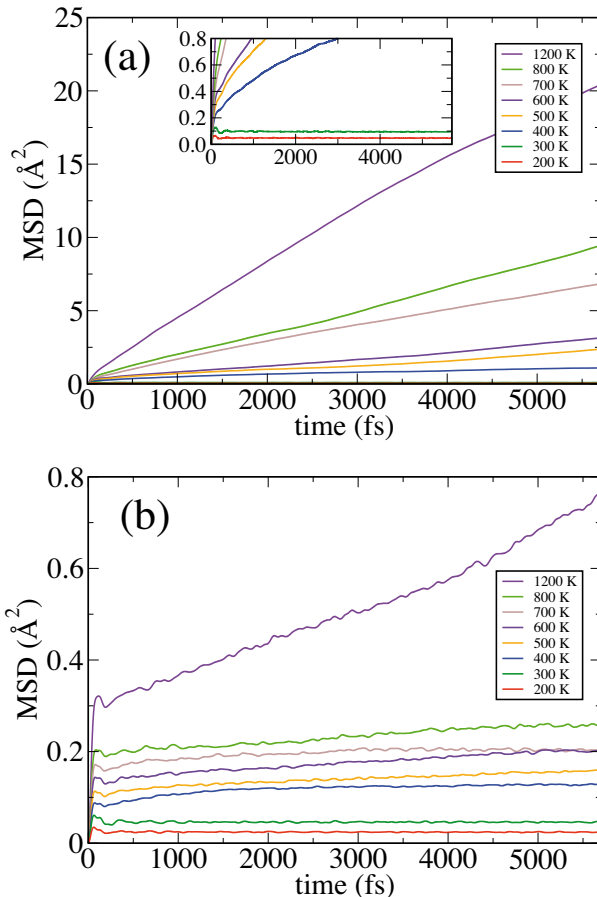


Figure 5.4: Mean square displacement for (a) Li and (b) N ions in the temperature range 200–1200 K. The inset for (a) shows the data for 200 K and 300 K in greater detail.

In Paper XIII, we have performed extensive *ab initio* molecular dynamics simulations of Li_2NH covering the temperature range from 200 K to 1200 K. The atomic forces were calculated using GGA-PW91 and PAW method. The structural phase transition was investigated by means of the pair distribution functions (PDF) and bond angles distributions averaged over 10000 fs. The Li-Li and N-N PDF curves within the studied temperature range are presented in Figures 5.3 (a) and (b), respectively. The former and latter provide information about the structures of cation and anion sub-lattices, respectively. One can observe that the Li-Li PDF undergoes a drastic change as the temperature reaches 400 K. The overall structure of the PDF stays then essentially the same as the temperature is further raised all the way up to $T=1200$ K, with

only a further broadening of the peaks taking place. Analysis of the peak positions and also the integration of the first peak of Li-Li PDF indicates that Li ions prefer a simple cubic arrangement for $T > 400$ K. However, this structure corresponds only to a time-averaged distribution. In fact, further evidence supports our hypothesis that such change in the PDF curve is associated with the melting of the Li sub-lattice.

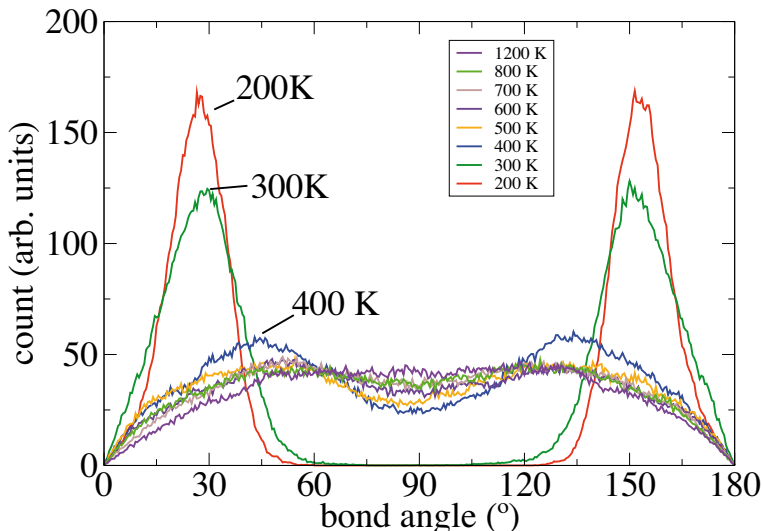


Figure 5.5: Bond angle distribution for the angles formed between N-H bonds and z-axis in the temperature range 200–1200 K.

The integration of the first N-N peak shows that each N atom is coordinated by 12 other N atoms, a characteristic feature of face-centered cubic (fcc) lattice. This nearest-neighbor peak is in fact composed of several sub-peaks which all merge into one narrow peak at 400 K, indicating a transition from a distorted fcc lattice to an essentially perfect one. The positions and heights of the second and third peaks further confirm that N atoms occupy a fcc lattice, which is in agreement with the experimental findings [96, 97, 98, 99, 101].

In Figures 5.4 (a) and (b), we present the mean square displacements as a function of time for the Li and N atoms, respectively. One can observe that as the temperature reaches 400 K, the MSD is clearly showing a finite slope, indicating diffusion of the Li ions in the system. Combining this information with the behavior of the Li-Li PDF curve, we conclude that Li sub-lattice undergoes a melting transition at around 400 K. This behavior would be hard to observe in x-ray diffraction experiments, rather it would appear like Li is located (on average) at the cubic lattice. However, it should be pointed out that the Li_2NH crystal as a whole is certainly not melting at a low temperature of 400 K. This will happen at around 900 K as observed from the MSD of N atoms in Figure 5.4 (b).

The melting of the Li sub-lattice is associated with a transition of the angle distribution of N-H bond (see Figure 5.5). As can be observed there is a order-disorder transition taking place at around 400K. For low temperatures, the partially positively charged H atoms bound to N in NH_2^- have to orient in a particular way to minimize repulsion from nearby positively charged Li ions. This ordering of the low-temperature phase is removed once the Li ions become mobile which in turn allows a more flexible arrangement for the H atoms.

This melting of the Li sub-lattice, may play an important role in the hydrogen sorption reactions involving Li_2NH . When Li_2NH reacts with H_2 to produce LiNH_2 plus LiH and also when it reacts with LiH to release hydrogen molecules forming Li_3N , an exchange between Li and H occurs with these atoms diffusing in the lattice. The models to explain this mechanism may now consider the new phase of the cation sub lattice.

6. Optical properties of saline hydrides

Light metals undergo a metal-insulator transition upon hydrogenation. This phenomenon highlight the importance of understanding their electrical and optical properties for a continuing technological development. In this chapter, the summary of our studies on crystalline MgH_2 and BeH_2 is presented. In the next two sections, it is discussed how to calculate the complex dielectric function and the GW quasiparticle energies. The results are in sections 6.3 and 6.4.

6.1 Complex dielectric function

The electric displacement field, \mathbf{D} , of a solid interacting with a monochromatic light beam, within a first-order linear approximation, can be written as

$$\mathbf{D} = \varepsilon(\omega, \mathbf{q})\mathbf{E}, \quad (6.1)$$

where ω , \mathbf{q} and \mathbf{E} refer to the frequency, wave vector and electric field of the electro-magnetic wave, respectively. The coupling constant, $\varepsilon(\omega, \mathbf{q})$, termed complex dielectric function, determines the response of the solid to the applied external field and can be determined experimentally.

The absorption of photons in a solid induces two kinds of electronic excitations, namely interband and intra-band electronic transitions. In the former, the electron is excited from the top of a fully filled band (valence band) to the bottom of an empty band (conduction band) while in the latter, the excitation occurs within the same band. The optical properties calculations presented in this thesis dealt with wide-band gap semiconductors, which display only interband transitions.

The first-principles calculations of the complex dielectric function can be performed using perturbation theory where the unperturbed part of the Hamiltonian is the crystal Hamiltonian and the light field is treated as the perturbation [102, 103]. On top of that the electric dipole approximation is employed and the imaginary part of the dielectric function becomes [104, 105]

$$\varepsilon_2^{ij}(\omega) = \frac{4\pi^2 e^2}{\Omega m^2 \omega^2} \sum_{\mathbf{k}nn'} \langle \mathbf{k}n' | p^i | \mathbf{k}n \rangle \langle \mathbf{k}n' | p^j | \mathbf{k}n \rangle \delta(E_{\mathbf{k}n'} - E_{\mathbf{k}n} - \hbar\omega), \quad (6.2)$$

where \mathbf{p} is the momentum operator, e is the electron charge, m its mass, Ω is the volume of the crystal and $|\mathbf{k}n\rangle$ is the crystal wavefunction corresponding to the n^{th} eigenvalue $E_{\mathbf{k}n}$ with crystal wave vector \mathbf{k} . The matrix elements

of the momentum operator give the probability of transitions between occupied and unoccupied states constrained to some selection rules. For example, the transition is allowed to take place between two states displaying angular momentum quantum number difference of ± 1 , which guarantees angular momentum conservation.

The real part of the dielectric function is calculated from ϵ_2 by performing the Kramers-Kronig transformation

$$\epsilon_1(\omega) = 1 + \frac{2}{\pi} \int_0^\infty d\omega' \epsilon_2(\omega') \left(\frac{\omega'}{\omega'^2 - \omega^2} \right). \quad (6.3)$$

This integral has to be evaluated using a frequency cut-off several times larger than the frequency range of interest in order to get accurate results.

When one use the density functional theory to calculate the complex dielectric function the eigen-states, $|\mathbf{k}n\rangle$, in (6.2) become the Kohn-Sham orbitals. It is well known that DFT does not provide good results for this kind of excitation spectra due to the fact that it is incapable of a proper treatment of the excited states. For instance, the band gap is under-estimated by about 30%-50%. One approach to make more quantitative comparison with the experimental findings is to perform a rigid shift of the calculated spectra upward in the photon energy in order to match the experimental band gap. This approach assumes that all eigen-energies can be corrected by the same value, within a given band, regardless at which k-point. To provide better treatment of all excited states, one has in fact to go beyond DFT. One first-step toward achieving this goal is to use the GW approximation. This method is explained in the next section.

6.2 GW quasi-particle

GW approximation is the first-step beyond DFT to treat more properly the excited electronic states in atoms, molecules and solids. This is an approximation for Hedin's equations [106] where vertex corrections are neglected leading to a self-energy that is given by the product of the dynamical screened interaction W and the Green's function G . Within this formalism, the quasi-particle (QP) eigenvalues $\epsilon_n(k)$ and eigenfunctions $\psi_{k,n}(\mathbf{r})$ are calculated by solving the following QP equation [106, 107].

$$(T + V_{ext} + V_h)\psi_{k,n}(\mathbf{r}) + \int d\mathbf{r}' \Sigma(\mathbf{r}, \mathbf{r}', E_n(\mathbf{k}))\psi_{k,n}(\mathbf{r}) = E_n(\mathbf{k})\psi_{k,n}(\mathbf{r}), \quad (6.4)$$

where T is the free-electron kinetic energy operator, V_{ext} is the external potential due to ion cores, V_h is the average electrostatic (Hartree) potential, and Σ is the electron self-energy operator, which is writtens as

$$\Sigma(\mathbf{r}, \mathbf{r}', \omega) = \frac{i}{2\pi} \int d\omega' G(\mathbf{r}, \mathbf{r}', \omega + \omega') e^{i\delta\omega'} W(\mathbf{r}, \mathbf{r}', \omega'). \quad (6.5)$$

In (6.5), G is the one-electron Green's function, δ is a positive infinitesimal and W is the screened Coulomb interaction, written as a product between the Coulomb potential and the inverse of the dielectric function ϵ . In the GW calculations presented in this thesis, the latter was calculated within the plasmon-pole approximation [108], which is computationally less expensive and provides similar results as the full GW when it is applied for sp bonded materials [109]. By treating $\Sigma - V_{xc}^{LDA}$ as a perturbation to the Kohn-Sham Hamiltonian H_{KS} , the real part of QP eigenvalues can be written as

$$ReE_n(\mathbf{k}) = \epsilon_n(\mathbf{k}) + Z_{nk} [\langle \Psi_{k,n} | Re\Sigma(\mathbf{r}, \mathbf{r}', \epsilon_n(\mathbf{k})) | \Psi_{k,n} \rangle - \langle \Psi_{k,n} | V_{xc}^{LDA} | \Psi_{k,n} \rangle]. \quad (6.6)$$

with

$$Z_{nk} = \left[1 - \langle \Psi_{k,n} | \frac{\partial}{\partial \omega} Re\Sigma(\mathbf{r}, \mathbf{r}', \epsilon_n(\mathbf{k})) | \Psi_{k,n} \rangle \right]^{-1}. \quad (6.7)$$

The eigenvalues $\epsilon_n(\mathbf{k})$ and the eigenfunctions $\Psi_{k,n}(\mathbf{r})$ in the equations above were obtained by solving the Kohn-Sham equation within the framework of either LDA or GGA by using the PAW method. More details about GW approximation can be found in the review article by Onida *et al.* [110].

6.3 MgH₂

The discovery of the optical transmission due to hydrogenation in rare-earth elemental metals [8] as well as in rare-earth-Mg [111]-[113] and MgNi [114] alloy thin films has driven the attention of the scientific community to investigate the optical properties of MgH₂. The transmission spectra of these alloys are shifted to higher energies with increasing Mg concentration, an effect explained by considering the formation of MgH₂, a wide band gap compound.

MgH₂ undergoes several pressure-induced phase transitions [115]-[117]. The ground state α -MgH₂ (TiO₂-rutile-type) transforms into orthorhombic γ -MgH₂ (α -PbO₂-type) at 0.39 GPa and the subsequent phase transformation from γ - to β -MgH₂ (Mod. CaF₂-type) occurs at 3.84 GPa. These phases can be found as a by-product in high-pressure syntheses of metal hydrides. For instance, in fully hydrogenated Y-Mg alloys, Nagengast *et al.* [118] have found that fcc YH₃ coexists with γ -MgH₂. Thus, to figure out the role of MgH₂ in Mg-based alloys, it is essential to determine the electronic and optical properties of their high-pressure phases.

In Papers XIV and XV, we present our studies on the electronic and optical properties of α -, γ - and β -phases of MgH₂. We have found an indirect GW band-gap of 5.58 eV for α -MgH₂, which agrees very well with the experimental findings [119]. The indirect (direct) GW band gap for the γ - and β -phases are found to be 5.24 eV (5.33 eV) and 3.90 eV (4.72 eV), respectively. The GW corrections are found to be almost constant for different k-points for a specific band. This result justifies the use of the scissor operator to correct the complex dielectric function by applying a rigid shift of the bands upward in

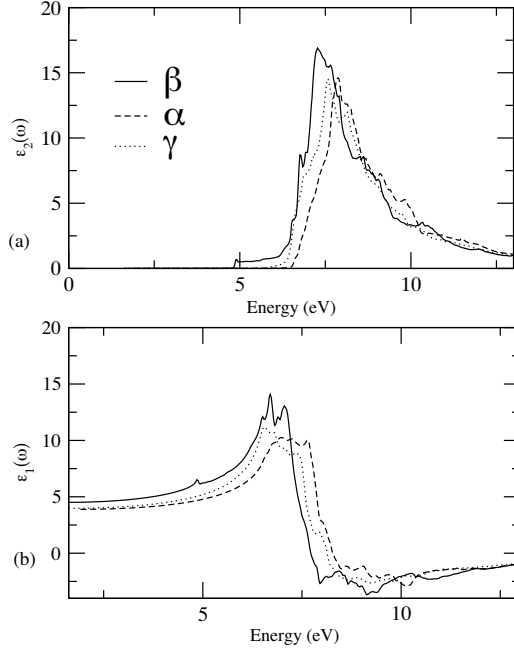


Figure 6.1: (a) Imaginary and (b) real part of the dielectric function. Dashed, dotted and solid lines represent the α -, γ -, and β -phase, respectively. The corrections by the scissor operation are included.

the photon energy. This is actually what we have employed here. The complex dielectric functions, calculated using FP-LAPW method, were shifted by an amount given by the difference between GGA and GW band-gaps. The real and imaginary part of the complex dielectric functions are shown in Figure 6.1. In spite of the observed band gap narrowing when going from the α -phase to the γ -phase and to the β -phase, we have found that β -MgH₂ displays a low absorption profile in the energy window 4.8-6.1 eV, which is a consequence of its low density of states on the top of the valence band. Therefore, its main absorption edge lies nearly at the same energy as those for the lower pressure phases (see Figure 6.1 (a)) showing that a significant modification of the light absorption spectrum may not be observed by the stabilization of this meta-stable higher pressure phase.

Finally, assuming the ratio of $\epsilon_1^c(0)/\epsilon_1^a(0)$ as a measure for the average optical anisotropy, where $\epsilon_1^c(0)$ and $\epsilon_1^a(0)$ are the static components of the real part of the dielectric constant along the c - and a -axes of the crystal, respectively. We claim that neither α -MgH₂ ($\epsilon_1^c(0)/\epsilon_1^a(0) = 1.01$) nor γ -MgH₂ ($\epsilon_1^c(0)/\epsilon_1^a(0) = 1.04$) show high anisotropy.

6.4 BeH₂

In Paper XVI, we investigate the electronic structure and optical properties of BeH₂, a parent compound of MgH₂, which may be considered as a candidate material for applications on both switchable mirrors and hydrogen storage if hurdles related to its high level of toxicity could be overcome.

The DFT part of the calculations have been performed using PAW method and GGA-PBE functional. In the low-pressure phase, this compound crystallizes in the *Ibam* space group with 18 atoms in a primitive cell. We have used here the experimental lattice and internal parameters without performing any geometry optimization.

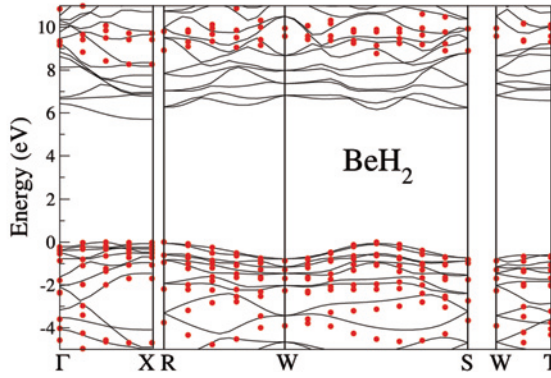


Figure 6.2: GGA band structure (full lines) and quasiparticle corrections (red dots) for BeH₂. The highest valence-band eigen-values are set at zero energy.

In Figure 6.2, we present the GGA and GW band structures along some high-symmetry directions of the Brillouin zone. As can be seen, BeH₂ is a direct band gap insulator. The values of the band gap are found to be 5.78 eV within the GGA and 8.27 eV within the GW approximation. Our GGA result is in good agreement with the theoretical GGA band-gap of 5.51 eV reported in Ref. [120].

The close inspection of the GW corrections revealed that for the conduction band states there may be different localization of electrons as a function of k -points. This could make the use of the scissor operator less precise. Nevertheless, this approach is still applied here in order to avoid the time-consuming computation of GW quasiparticles energies and bands. We have rigidly shifted the calculated dielectric function by 2.49 eV (difference between GGA and GW band-gaps) upward in photon energy. The results are presented in Figure 6.3. As can be seen the shape of the imaginary part is characterized by a sharp increase between 9 and 10 eV, corresponding to a sudden increase of the number of available transitions around this energy. This can be seen also

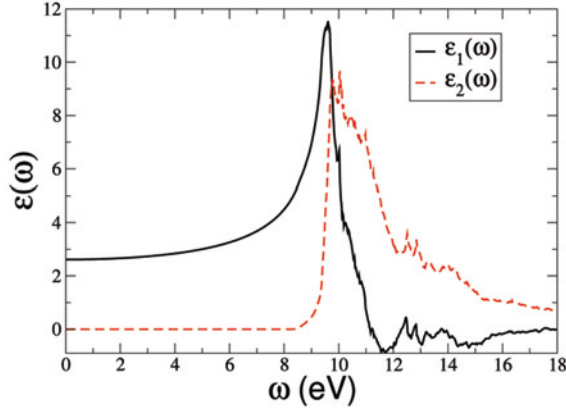


Figure 6.3: Real ($\epsilon_1(\omega)$) and imaginary ($\epsilon_2(\omega)$) dielectric functions for BeH₂ averaged over the three non-equivalent directions.

from the band structure. The other satellite peaks are difficult to correlate with the band structure due to the high number of bands lying in the same range of energy.

In summary, we have found that BeH₂ is a wide band-gap insulator with a direct band gap of 8.27 eV. From the calculated dielectric function it was found that the allowed transitions starts at around 9 eV. We hope that this work will stimulate more experiments on this topic. In particular, the results presented here can be directly compared to photoemission experiments as well as optical spectroscopy.

7. Conclusions and outlook

In this thesis, we have extensively used first-principles calculations to understand the properties of potential hydrogen storage materials. A number of systems have been studied including for instance sodium alanate, sodium borate, amides, imides, magnesium dihydride and metal-organic frameworks.

The results of our investigations on MgH_2 nano-clusters doped with various transition metals (TM) supports the gateway hypothesis for the catalysis mechanism where the transition metals keep continuously attracting new hydrogen atoms from the rest of the cluster as hydrogen desorbs. In addition, it was found that iron diffuses upon dehydrogenation moving toward hydrogen-rich regions, suggesting that it may stay in the MgH_2/Mg interface region continuously catalyzing the dehydrogenation process. This effect may also occur for the other TM. To further understand this mechanism, it would be worth to employ molecular dynamics simulations at temperatures equivalent to the ones used in the experiments.

In NaAlH_4 doped with 3d transition metals, we have found that hydrogen atoms display diminished binding energies and higher mobility, when compared with the pure compound, due to the formation of TM-Al bonds, a result supporting the hypothesis of TM-Al intermetallic formation as the main catalytic mechanism for the hydrogen sorption reaction. The same effect is also predicted to occur in Ti-doped NaBH_4 . Furthermore, we predict that Cr and Fe may be more effective than Ti to catalyze NaAlH_4 . The presence of Na vacancies are also shown to significantly diminish the hydrogen binding energy in sodium alanate. The increase of the concentration of such defect is assumed to be due to the reaction between TiCl_3 and NaAlH_4 . It should also be noted that, techniques used to create nano-particles like ball milling, which operate under non-equilibrium conditions, are also able to significantly increase the concentration of such defects.

We have performed a systematic investigation of the hydrogen storage properties of $\text{Mg}(\text{NH}_2)_2\text{-LiH}$ mixtures. For the three mixing $\text{LiH}/\text{Mg}(\text{NH}_2)_2$ ratios of 2/1, 8/3 and 12/3, the hydrogen release process is initiated by the same reaction with an enthalpy of $46.1 \text{ kJ (mol of H}_2\text{)}^{-1}$. The remaining hydrogen is released in one extra step for the ratio of 8/3 and two extra steps for the ratio of 12/3, which display significantly higher enthalpies. Thus, while the weight percentage of hydrogen stored in the respective reactions with various mixing ratios differs, the actual amount of hydrogen gas released at the lowest (and presumably only practical) temperature remains the same. It should be pointed out that the main obstacle in the earlier stage of these studies was the determination of the crystal structure of some chemical hydrides, in particu-

lar of $\text{Li}_2\text{Mg}(\text{NH})_2$. The resolution of hydride crystal structures is in fact a challenging task that can greatly benefit from a symbiosis between theory and experiment.

In the metal-organic framework-5 (MOF-5), it was found that by adsorbing Li atoms on the organic linkers, the H_2 binding energy is significantly raised, which enhances the hydrogen gas uptake properties. In fact, we show from molecular dynamics simulations with a hydrogen loading of 18 H_2 per formula unit that a hydrogen uptake of 2.9 wt% at 200 K and 2.0 wt% at 300 K may be achievable. One next step would be the investigation of the effect of coating MOFs with other chemical elements such as 3d transition metals. In this case, the interaction between 3d orbitals and hydrogen σ bond could rise the H_2 binding energy even further. However, our preliminary results for Sc and Ti showed that metal clustering in the center of the pore is energetically favored. Therefore, we believe that the best approach is indeed to use light alkali and alkaline earth metals for which such clustering is deemed unlikely based on our results.

Lastly, the following studies were also carried out. We investigated pressure-induced structural phase transformations of NaBH_4 and ErH_3 . In the latter, an electronic transition is shown to accompany the structural modification. The electronic and optical properties of the low and high-pressure phases of crystalline MgH_2 were calculated. The temperature-induced order-disorder transition in Li_2NH was investigated by extensive molecular dynamics simulations. Here, it is demonstrated that the structural phase transformation is triggered by Li sub-lattice melting. This result may contribute to further understand important solid-solid hydrogen storage reactions that involve this compound. Furthermore, our results show a complete melting at around 900 K.

In spite of the significant progress already achieved by the scientific community toward designing suitable hydrogen storage systems for mobile applications, there still are many hurdles that need to be overcome. This thesis has shown how first-principles calculations can contribute to a better understanding of a number of aspects related to hydrogen storage materials and may even lead the way in some cases to inspire new experiments. We believe that the greatest progress will come from research efforts resulting from a close collaboration between theory and experiments.

Acknowledgments

First of all, I would like to thank my supervisor Rajeev Ahuja for accepting me as PhD student in the group. His support, encouragement and guidance have been very important for my studies. I would like also to thank Puru Jena at Virginia Commonwealth University for introducing me to investigations of catalyzed sodium alanate.

My move to Sweden became much simpler than it was supposed to be thanks to Jailton, a great friend who was already living here. Jai, thank you very much for all help at that time, and, more importantly, for many years of friendship! I would like to thank Antonio Ferreira da Silva primarily for his friendship and also for always giving me support whenever I needed. Thank you for everything! I would like to thank Adriano, a close friend, who has always motivated my studies in Physics. I would like also to thank all brazilian friends that I have met in Uppsala. They have made our life much easier.

I have done most of my work in collaboration with many people from which I have learned a lot. Ralph, thank you for the fruitful collaboration during the last years and also for being so kind whenever I come with my questions/suggestions. Our work has been benefited a lot from your positive attitude. I promise, I will think about the environment before printing something (smiles). I should admit, that was a good lesson from you. Anden, thank you for making our work so productive. I appreciate very much our everyday discussions and your enthusiasm to implement whatever idea we come up with. Thanks also for the good time during our long trips. Peter, thank you for our good collaboration on the cluster calculations. Our discussions helped me to broaden my understanding of that problem. Thank you also for being available to help me whenever I had a problem with my mac, and also for the good suggestions to improve its usage. Juck, the collaboration with you is also very much appreciated. Thank you. Duck, first of all I would like to thank you for the sushi tutorial, it was a great time. It is being really enjoyable to have you around and to collaborate with you as well. Cecilia, thank you for our collaboration, it is being a good challenge (smiles). I would also like to thank Sebastien for the collaboration in the investigations of the electronic and optical properties of hydrogen storage materials and also for the fruitful discussions about Physics in general.

Specially, I would like to thank very much again Ralph, Peter, Anden and Cecilia for the critical reading of this thesis providing valuable suggestions and comments. Your help will not be forgotten! Anden and Cecilia, thank you very much also for the translation of the summary in Swedish.

Now some other people that have also being important. First, many thanks go to Clas Persson who strongly recommended me to come to Uppsala for my PhD. Clas, thank you also for teaching me with patience the first *ab initio* method that I have used, LAPW. Sergiu, thank you for helping me in getting started with the phonon code and also for always being open for discussions. Moreno, thank you for the nice chats during coffee breaks. Many thanks for Lisa, Lunmei and Jorge who helped me very much in the beginning of my work. Many thanks go also to Erik for your kindness and friendship. You have helped me a lot by proving useful practical informations when I moved to Uppsala. I hope our recently initiated collaboration will produce good results. I would like to thank also Raquel for the great help when I got to Uppsala. I would like to thank Love for the good time when we were roommates. I would like to thank Pooja and Dianna for the nice dinners and enjoyable time for me and my wife. I should not forget to thank Thomas, Peter, Anders, Weiner, Björn, Lars B, Carlos, Alexei and all other people who worked to keep the computers running. I would like to acknowledge Börje Johansson for the special atmosphere of our group. I would like to thank Elisabeth for all help with the administrative work. And also, a warm thanks for all members in the group. This is really an enjoyable place to work in.

Finally, last but not least, I would like to thank my family, but in the proper language (smiles). Mile, meu amor, muito obrigado por ter acreditado neste sonho e por todo apoio ao longo desta jornada, te amo. Meus queridos familiares o apoio de voces foi muito importante para que tudo isso se tornasse uma realidade, muito obrigado pelo amor e carinho de todos voces. Amo a todos!

8. Sammanfattning på Svenska

Väte är ett av de grundämnen som det finns rikligt av här på jorden. Väte kan genom en kemisk reaktion med O_2 avge energi med endast vatten som biprodukt och används därför bland annat i förbränningsmotorer och bränsleceller. På grund av denna egenskap ses väte som en möjlig ersättare för dagens miljöfarliga fossila bränslen. Fossila bränslen kommer inte att kunna tillgodose framtidens världsomspännande krav på en hållbar energiutveckling. Dock finns inte väte tillgängligt i ren gasform utan är bundet till andra grundämnen i till exempel vatten och organiska molekyler. Därför är en av förutsättningarna för en utbredd användning av väte som drivmedel (även kallad väteekonomin) utvecklingen av effektiva metoder för att producera vätgas [1]. Ett andra hinder som måste övervinnas för att möjliggöra användningen av väte som drivmedel i fordon är lagringen av väte [1,2]. Detta är den huvudsakliga problemställningen som behandlas i denna avhandling.

För att ett vätelagringssystem skulle vara användbart i fordon krävs att följande sex grundförutsättningar, baserade på ekonomiska och miljömässiga hänsynstaganden, uppfylls:

- (i) Hög mass- och volymtätethet ($> 4,5$ viktprocent väte och > 36 g H_2/L),
- (ii) En arbetstemperatur mellan $60\text{ }^\circ C$ och $120\text{ }^\circ C$ vid låga tryck (kring 1 bar),
- (iii) En reversibel absorptions- och desorptionscykel för vätet,
- (iv) Låg kostnad för materialet,
- (v) Ej giftigt och
- (vi) Säkert.

En lovande inriktning i sökandet efter ett sådant system är att lagra vätet i kristallgittret hos ett material. Denna metod undersöks på grund av att vätelagring under högt tryck och i vätskeform vid låga temperaturer inte är tillräckligt effektiva. Förutom säkerhetsaspekterna och kostnaderna för att komprimera eller kyla ned vätgas, är energitätheten hos vätgas vid 700 bar ($4,4$ MJ/L) och flytande väte vid 20 K (8 MJ/L) lägre än energitätheten hos bensen. Hos några övergångsmetaller, till exempel Nb och V, sker vätets desorptions- och adsorptionscykel vid tryck och temperaturer som tillgodoser krav (ii). Dock är vätets masstäthet i dessa övergångsmetaller sällan högre än tre viktprocent, vilket gör att krav (i) inte uppfylls. För att kunna lagra mer än sex viktprocent väte krävs att lagringsmaterialet består av lätta grundämnen. Därför har stor vikt lagts vid forskning på lättmetallhydrider (LMH) som aluminiumföreningar ($KAlH_4$, $NaAlH_4$, $LiAlH_4$) borföreningar (KBH_4 , $NaBH_4$, $LiBH_4$), litium-kväveföreningar ($LiNH_2$ - Li_2NH)[4] och magnesiumföreningar (MgH_2)[2]. Dessa LMH har hög viktandel väte, upp till 18 viktprocent hos $LiBH_4$. En av nackdelarna med LMH är att

väteatomerna är bundna av starka jonbindningar och kovalenta bindningar vilket resulterar i ofördelaktig termodynamik och kinetik i desorptions- och absorptionscykeln. Trots detta ses materialen ändå som lovande för vätelagring tack vare utvecklingen av nya metoder för att destabilisera dem.

För att förbättra vätelagringsegenskaperna hos LMH används för tillfället följande tillvägagångssätt: tillsatser av katalysatorer, syntetisering av nanopartiklar samt blandningar av olika hydridfaser. I denna avhandling behandlas olika problemställningar sammankopplade till dessa tre metoder med hjälp av kvantmekaniska beräkningar. Vi har till exempel undersökt effekterna av orenheter på vätedesorptionen i 3d-övergångsmetall-dopade NaAlH_4 , NaBH_4 och MgH_2 nanokluster samt även termodynamiken hos vätetets desorption och absorption i Li-Mg-N-H system där fasen fylld med väte består av en blandning av $\text{Mg}(\text{NH}_4)_2$ och LiH. I fallet med NaAlH_4 stöder våra resultat förklaringen att bildandet av intermetalliska legeringar, M-Al, är en av de viktigaste bidragen till den katalytiska effekten. Detta visas även vara fallet för Ti i NaBH_4 . För MgH_2 nanokluster stöder de observerade yteffekterna av övergångsmetaller en slussningshypotes för väteavgivning där övergångsmetallerna kontinuerligt attraherar nya H atomer från resten av nanoklustret allt eftersom H atomer avges. Dessutom upptäcktes att Fe diffunderar mot väterika områden när väte avges vilket implicerar att Fe, och troligtvis andra övergångsmetaller, kan stanna i gränsområdet mellan Mg och MgH_2 där det kontinuerligt kan fungera som en katalysator för vätedesorptionen. Vidare har vi för blandningen av $\text{Mg}(\text{NH}_4)_2$ och LiH funnit att en ökning av halten LiH inte leder till en förbättrad vätgasdesorption ifall inte temperatur- eller tryckförutsättningarna ändras. Den totala desorptionen av väte sker stegvis, och kräver högre och högre temperaturer för varje steg.

Ett alternativ till lagring i LMH är att lagra molekyllärt väte på väggarna i högytematerial. En stor fördel med denna metod är att kinetiken för H adsorption och desorption är snabb. Orsaken till detta är att inga kemiska bindningar förändras när vätet binds till materialet. Emellertid är det även denna egenskap som gör att det krävs väldigt låga temperaturer för att hålla kvar väte som binds av svaga van der Waals krafter. Det finns många material som kan lagra väte på detta sätt, exempel är kolnanorör [5], molekyllära clathrates [6] och metallorganiska nätverk [7]. I den här avhandlingen har vi undersökt vätelagringsegenskaperna hos metallorganiska nätverk. Vi har med hjälp av kvantmekaniska beräkningar bestämt adsorptionsenergierna för vätemolekyler vid olika positioner på porväggarna. Denna information är viktig för att förstå mekanismerna bakom bindningen av molekyllärt väte i heterogena system. Vidare visar vi hur tillsatsen av Li atomer på porväggarna flerfaldigt förstärker bindningarna mellan ytan och vätet. Som exempel visar vi att det är möjligt att lagra upp till två viktprocent väte vid en temperatur på 300 K och lågt tryck. Detta är den högsta lagringskapacitet som upptäckts för denna typ av system vid dessa förhållanden.

Vid sidan om vätelagring är metall-väte system intressanta i andra teknologiska applikationer tack vare stora förändringar i deras fysiska egenskaper beroende på närvaron av väte [8]. Ett exempel är Mg som vid absorption

av väte genomgår en övergång från metall till isolator och samtidigt även övergår från att vara en skinande metall (Mg) till att vara en genomskinlig bredbandig halvledare (MgH_2). Samma effekt återfinns även i Y metall där följande sekvens sker: Y (metallisk) - YH_2 (metallisk) - YH_3 (halvledande). Dessa växlingsbara speglar kan användas i applikationer som smarta fönster. Detta är även av intresse i vår undersökning av högtrycksfasen hos MgH_2 . Det huvudsakliga resultat är att kanten av den imaginära delen hos den dielektriska funktionen, där ljusadsorption initieras, inte påverkas av de metastabila högtrycksfaserna. Denna information är viktig vid design av nya optiska apparater med denna metallhydrid.

Egenskaperna hos metallhydrider kan finjusteras genom att använda fasövergångar som sker på grund av förändringar i tryck och/eller temperatur. Förståelsen av den bakomliggande fysiken hos dessa fenomen är viktig både ur en grundforsknings och även ur en mer applicerad synvinkel. Vi har undersökt sådana fasövergångar i tre viktiga hydrider nämligen NaBH_4 , Li_2NH och ErH_3 . NaBH_4 genomgår en strukturell fasövergång från en kubisk struktur till en monoklin struktur vid ett beräknat tryck på 19 GPa, vilket överensstämmer bra med det experimentellt bestämda övergångstrycket på 15 GPa. Kristallstrukturen hos ErH_3 övergår från en hexagonal struktur till en kubisk struktur vid ett tryck på 17 GPa. Vid denna strukturella övergång sker även en övergång från metall till isolator. Ett viktigt resultat hittades gällande strukturella övergångar i Li_2NH där en fasövergång visade sig vara utlöst av smältningen hos katjon-gittret kring 400 K. Detta resultat kan bidra till förståelsen av den kemisk fasta tillståndets reaktion mellan Li_2NH och LiH som avger vägas.

Bibliography

- [1] G. W. Crabtree, M. S. Dresselhaus and M. V. Buchanan, *Physics Today* **39**, (December-2004).
- [2] L. Schlappbach and A. Züttel, *Nature* **414**, 353 (2001).
- [3] W. Grochala and P. P. Edwards, *Chem. Rev.* **104**, 1283 (2004).
- [4] S. Orimo, Y. Nakamori, J. R. Eliseo, A. Züttel and C. M. Jensen, *Chem. Rev.* **107**, 4111 (2007).
- [5] A. C. Dillon and M. J. Heben, *Appl. Phys. A* **72**, 133 (2001).
- [6] V. V. Struzhkin, B. Militzer, W. L. Mao, H. Mao and R. J. Hemley, *Chem. Rev.* **107**, 4133 (2007).
- [7] J. L. C. Rowsell and O. M. Yaghi, *Angew. Chem. Int. Ed.* **44**, 4670 (2005).
- [8] J. N. Huibert, R. Griessen, J. H. Rector, R. J. Wijngaarden, J. P. Dekker, D. G. De Groot and N. J. Koeman, *Nature* **380**, 231 (1996).
- [9] P. Hohenberg and W. Kohn, *Phys. Rev.* **136**, B864 (1964).
- [10] W. Kohn and L. Sham, *Phys. Rev.* **140**, A1133 (1965).
- [11] Richard M. Martin, *Electronic Structure Basic Theory and Practical Methods* (Cambridge University Press, 2004).
- [12] D. M. Ceperley and B. J. Alder, *Phys. Rev. Lett.* **45**, 566 (1980).
- [13] A. D. Becke, *Phys. Rev. A* **38**, 3098 (1988).
- [14] J. P. Perdew and Y. Wang, *Phys. Rev. B* **45**, 13244 (1992).
- [15] J. P. Perdew, K. Burke and M. Ernzerhof, *Phys. Rev. Lett.* **77**, 3865 (1996).
- [16] J. Tao, J. P. Perdew, V. N. Staroverov and G. E. Scuseria, *Phys. Rev. Lett.* **91**, 146401 (2003).
- [17] N. W. Ashcroft and N. David Mermim, *Solid State Physics*, Saunders College Publishing, 1976.
- [18] S. Cottenier, *Density Functional Theory and the family of (L)APW-method a step-by-step introduction* (Instituut voor kern-en Stralingsfysica, K. U. Leuven, Belgium), 2002, ISBN 90-807215-1-4 (to be found at <http://www.wien2k.at/reg-user/textbooks>).
- [19] J. C. Slater, *Phys. Rev.* **51**, 846 (1937).

- [20] O. K. Andersen, Phys. Rev. B **12**, 3060 (1975).
- [21] D. J. Singh, Planewaves, pseudopotentials and the LAPW method (Kluwer Academic Publishers Massachusetts, 1994).
- [22] P. Blaha, K. Schwarz, G. K. H. Madsen, D. Kvasnicka, and J. Luitz, WIEN2k, An Augmented Plane Wave + Local Orbitals Program for Calculating Crystal Properties (Karlheinz Schwarz, Techn. University Wien, Austria), 2001, ISBN 3-9501031-1-2.
- [23] P. E. Blöchl, Phys. Rev. B **50**, 17953 (1994).
- [24] G. Kresse and J. Hafner, Phys. Rev. B **47**, R558 (1993).
- [25] D. Vanderbilt, Phys. Rev. B **41**, 7892 (1990).
- [26] A. Szabo and N. S. Ostlund, Modern Quantum Chemistry: Introduction to Advanced Electronic Structure Theory (McGraw-Hill, Inc., 1989).
- [27] A. Köhn, F. Weigend and R. Ahlrichs, Phys. Chem. Chem. Phys. **3**, 711 (2001).
- [28] R. Ahlrichs, M. Bär, H. Horn and C. Kölmel, Chem. Phys. Lett. **162**, 165 (1989).
- [29] J. M. Haile, Molecular Dynamics Simulations - Elementary Methods, John Wiley Sons, Inc., New York, 1992.
- [30] V. Bérubé, G. Radtke, M. Dresselhaus and G. Chen, Int. J. Energy Res. **31**, 637 (2007).
- [31] X. Ke and I. Tanaka, Phys. Rev. B **71**, 024117 (2005).
- [32] F. E. Pinkerton and B. G. Wicke, The Industrial Physicist, 20 (2004).
- [33] A. Zaluska, L. Zaluski and J. O. Ström-Olsen, J. Alloys Compd. **288**, 217 (1999).
- [34] G. Liang, J. Huot, S. Boily, A. Van Neste and R. Schulz, J. Alloys Compd. **292**, 247 (1999).
- [35] J. F. Pelletier, J. Huot, M. Sutton, R. Schulz, A. R. Sandy, L. B. Lurio, and S. G. J. Mochrie, Phys. Rev. B **63**, 052103 (2001).
- [36] J. Hout, G. Liang, S. Boily, A. Van Neste, R. Schulz, J. Alloys Comp. **293**, 495 (1999).
- [37] J. F. Pelletier, J. Huot, M. Sutton, R. Schulz, A. R. Sandy, L. B. Lurio, S. G. J. Mochrie, Phys. Rev. B **63**, 052103 (2001).
- [38] B. Bogdanovic, and M. Schwickardi, J. Alloys Comp. **253**, 1 (1997).
- [39] K. J. Gross, S. Guthrie, S. Takara and G. Thomas, J. Alloys. Compd. **297**, 270 (2000).
- [40] K. J. Gross, G. J. Thomas and C. M. Jensen, J. Alloys and Comp. **330**, 683 (2002).

- [41] D. L. Sun, T. Kiyobayashi, H. T. Takeshita, N. Kuriyama, and C. M. Jensen, *J. Alloys. Compd.* **337**, L8 (2002).
- [42] H. W. Brinks, B.C. Hauback, P. Norby and H. Fjellvåg, *J. Alloys Compd.* **351**, 222 (2003).
- [43] P. Wang, and C. M. Jensen, *J. Alloys Compd.* **379**, 99 (2004).
- [44] B. C. Hauback, H. W. Brinks, C. M. Jensen, K. Murphy, and A. J. Maeland, *J. Alloys Compd.* **358**, 142 (2003).
- [45] H. W. Brinks, C. M. Jensen, S. S. Srinivasan, B. C. Hauback, D. Blanchard and K. Murphy, *J. Alloys Compd.* **376**, 215 (2004).
- [46] R. T. Walters and J. H. Scogin, *J. Alloys Compd.* **379**, 135 (2004).
- [47] V. Ozolins, E. H. Majzoub and T. J. Udovic, *J. Alloys Compd.* **375**, 1 (2004).
- [48] B. Bogdanovic et al., *J. Alloys. Compd.* **350**, 246 (2003).
- [49] J. Graetz, J. J. Reilly, J. Johnson, A.Yu. Ignatov, and T. A. Tyson, *Appl. Phys. Lett.* **85**, 500 (2004).
- [50] P. Vajeeston, P. Ravindran, R. Vidya, H. Fjellvåg and A. Kjekshus, *Appl. Phys. Lett.* **82**, 2257 (2003).
- [51] J. Iniguez, T. Yildirim, T. J. Udovic, M. Sulic and C. M. Jensen, *Phys. Rev. B* **70**, 060101(R) (2004).
- [52] O. M. Løvvik and S. M. Opalka, *Phys. Rev. B* **71**, 054103 (2005).
- [53] A. Aguayo and D. J. Singh, *Phys. Rev. B* **69**, 155103 (2004).
- [54] O. M. Løvvik, *J. Alloys Comp.* **356**, 178 (2003).
- [55] W. Luo, and K. J. Gross, *J. Alloys Comp.* **358**, 224 (2004).
- [56] O. Palumbo, R. Cantelli, A. Paolone, C. M. Jensen and S. S. Srinivasan, *J. Phys. Chem. B* **109**, 1168 (2005).
- [57] Z. P. Li, N. Morigazaki, B. H. Liu and S. Suda, *J. Alloys Compd.* **349**, 232 (2003).
- [58] Z. P. Li, B. H. Liu, K. Arai, K. Asaba and S. Suda, *J. Power Sources* **126**, 28 (2004).
- [59] C. Wu, H. Zhang and B. Yi, *Catalysis Today* **93**, 477 (2004).
- [60] Z. P. Li, B. H. Liu, K. Arai, N. Morigazaki and S. Suda, *J. Alloys Compd.* **356**, 469 (2003).
- [61] V. Ozolins, E. H. Majzoub, and T. J. Udovic, *J. Alloys Compd.* **375**, 1 (2004).
- [62] E. H. Majzoub and K. J. Gross, *J. Alloys. Compd.* **356**, 363 (2003).
- [63] P. Chen, Z. Xiong, J. Luo, J. Lin, and K. L. Tan, *Nature* **420**, 302 (2002).

- [64] W. Luo, J. Alloys Compd. **381**, 284 (2004).
- [65] Z. Xiong, G. Wu, J. Hu, and P. Chen, Adv. Mater. **16**, 1522 (2004).
- [66] H. Y. Leng, T. Ichikawa, S. Hino, N. Hanada, S. Isobe, and H. Fujii, J. Phys. Chem. B **108**, 8763 (2004).
- [67] Y. Nakamori, G. Kitahara, K. Miwa, S. Towata, and S. Orimo, Appl. Phys. A **80**, 1 (2005).
- [68] J. Rijssenbeek, Y. Gao, J. Hanson, Q. Huang, C. Jones, and B. Toby, J. Alloys Compd. (2007), doi:10.1016/j.jallcom.2006.12.008. (In press; available online).
- [69] R. C. Lochan, M. Head-Gordon, Phys. Chem. Chem. Phys. **8**, 1357 (2006).
- [70] T. Yildirim and S. Ciraci, Phys. Rev. Lett. **94**, 175501 (2005).
- [71] Y. Zhao, Y. Kim, A. C. Dillon, M. J. Heben, and S. B. Zhang, Phys. Rev. Lett. **94**, 155504 (2005).
- [72] H. Lee, W. I. Choi and J. Ihm, Phys. Rev. Lett. **97**, 056104 (2006).
- [73] Q. Sun, Q. Wang, P. Jena and Y. Kawazoe, J. Am. Chem. Soc. **127**, 14582 (2005).
- [74] Q. Sun, P. Jena, Q. Wang, M. Marquez, J. Am. Chem. Soc. **128**, 9741 (2006).
- [75] J. L. C. Rowsell, A. R. Millward, K. S. Park, O. M. Yaghi, J. Am. Chem. Soc. **126**, 5556 (2004).
- [76] T. Yildirim and M.R. Hartman, Phys. Rev. Lett **95**, 215504 (2005).
- [77] T. Mueller and G. Ceder, J. Phys. Chem. B **109**, 17974 (2005).
- [78] A. Samanta, T. Furuta and J. Li, J. Chem. Phys. **125**, 084714 (2006).
- [79] H. K. Chae, D. Y. Siberio-Pérez, J. Kim, Y. Go, M. Eddaoudi, A. J. Matzger, M. O’Keeffe, O. M. Yaghi, Nature **427**, 523 (2004).
- [80] G. Férey, M. Latroche, C. Serre, F. Millange, T. Loiseau, A. Percheron-Guégan, Chem. Comm., 2976 (2003).
- [81] A. P. Côté and G. K. H Shimizu, Chem. Eur. J. **9**, 5361 (2003).
- [82] S. R. Batten and R. Robson, Angew. Chem. Int. Ed. **37**, 1460 (1998).
- [83] B. Chen, M. Eddaoudi, S. T. Hyde, M. O’Keeffe, O. M. Yaghi, Science **291**, 1021 (2001).
- [84] B. Chen, M. Eddaoudi, T. M. Reineke, J. W. Kampf, M. O’Keeffe, O. M. Yaghi, J. Am. Chem. Soc. **122**, 11559 (2000).
- [85] T. Sagara, J. Klassen, E. Ganz, J. Chem. Phys. **121**, 12543 (2001).
- [86] S. S. Han and W. A. Goddard III, J. Am. Chem. Soc. **129**, 8422 (2007).

- [87] K. L. Mulfort and J. T. Hupp, J. Am. Chem. Soc. **129**, 9604 (2007).
- [88] F. D. Murnaghan, Am. J. Math **49**, 235 (1937); F. D. Murnaghan, Proc. Natl. Acad. Sci. USA **30**, 244 (1944).
- [89] F. Birch, Phys. Rev. **71**, 809 (1947).
- [90] P. J. Kelly, J. P. Dekker, R. Stumpf, Phys. Rev. Lett. **78**, 1315 (1997).
- [91] R. Ahuja, B. Johansson, J. M. Wills, O. Eriksson, Appl. Phys. Lett. **71**, 3498 (1997).
- [92] R. J. Wijngaarden, J. N. Huiberts, D. Nagengast, J. H. Rector, R. Griessen, M. Hanfland and F. Zontone, J. Alloys Comp. **308**, 44 (2000).
- [93] A. Ohmura, A. Machida, T. Watanuki, K. Aoki, S. Nakano, and K. Takemura, Phys. Rev. B **73**, 104105 (2006).
- [94] J.S. de Almeida, D.Y. Kim, C. Ortiz, M. Klintenberg, R. Ahuja, *submitted to Phys. Rev. Lett.*.
- [95] T. Palasyuk and M. Tkacs, Solid State Commun. **130**, 219 (2004).
- [96] T. Ichikawa, N. Hanada, S. Isobe, H. Leng, and H. Fujii, J. Phys. Chem. B **108**, 7887 (2004).
- [97] J. F. Herbst and L. G. Hector, Jr., Phys. Rev. B **72**, 125120 (2005).
- [98] T. Noritake, H. Nozaki, M. Aoki, S. Towata, G. Kitahara, Y. Nakamori, and S. Orimo, J. Alloys Compd. **393** 264, (2005).
- [99] K. Ohoyama, Y. Nakamori, S. Orimo, and K. Yamada, J. Phys. Soc. Jpn. **74**, 483 (2005).
- [100] B. Magyari-Köpe, V. Ozolinš, and C. Wolverton, Phys. Rev. B **73**, 220101(R) (2006).
- [101] M. P. Balogh, C. Y. Jones, J. F. Herbst, L. G. Hector Jr., and M. Kundrat, J. Alloys Compd. **420**, 326 (2006).
- [102] Peter Y. Yu and Manuel Cardona, Fundamentals of Semiconductors Physics and Materials Properties (Springer, Berlin, 1996).
- [103] Otfried Madelung, Introduction to Solid State Theory (Springer, Berlin, 1996).
- [104] F. Bassani and G. Pastori Parravinci, Edited by R. A. Ballinger, (Pergamon Press, 1975).
- [105] C. Ambrosch-Draxl and J. O. Sofo, Comp. Phys. Comm., **175**, 1 (2006).
- [106] L. Hedin, Phys. Rev. **139**, A796 (1965).
- [107] L. Hedin and S. Lundqvist, Solid State Physics, **23** (1969), ed. H. Ehrenreich, F. Seitz and D. Turnbull (New York: Academic).

- [108] B. Arnaud and M. Alouani, Phys. Rev. B **62**, 4464 (2000).
- [109] S. Lebègue, B. Arnaud, M. Alouani and P. E. Bloechl, Phys. Rev. B **67**, 155208 (2003).
- [110] G. Onida, L. Reining and A. Rubio, Rev. Mod. Phys. **74**, 601 (2002).
- [111] P. Van der Sluis, M. Ouwerkerk, and P. A. Duine, Appl. Phys. Lett. **70**, 3356 (1997).
- [112] M. Ouwerkerk, Solid State Ionics **431**, 113 (1998).
- [113] I. A. M. E. Giebels, J. Isidorsson and R. Griessen, Phys. Rev. B **69**, 205111 (2004).
- [114] T. J. Richardson, J. L. Slack, R. D. Armitage, R. Kostecki, B. Farangis and M. D. Rubin, Appl. Phys. Lett. **78**, 3047 (2001).
- [115] P. Vajeeston, P. Ravindran, A. Kjekshus and H. Fjellvåg Phys. Rev. Lett. **89**, 175506 (2002).
- [116] J. P. Bastide, B. Bonnetot, J. M. Ltoff and P. Claudy, Mater. Res. Bull. **15**, 1215 (1980).
- [117] M. Bortz, B. Bertheville, G. Böttger and K. Yvon, J. Alloys Compd. **287**, L4 (1999).
- [118] D. G. Nagengast, A. T. M. van Gogh, E. S. Kooij, B. Dam and R. Griessen, Appl. Phys. Lett. **75**, 2050 (1999).
- [119] J. Isidorsson, I. A. M. E. Giebels, H. Arwin and R. Griessen, Phys. Rev. B **68**, 115112 (2003).
- [120] P. Vajeestone, P. Ravindran, A. Kjekshus and H. Fjellvåg, Appl. Phys. Lett. **84**, 34 (2004).

Acta Universitatis Upsaliensis

*Digital Comprehensive Summaries of Uppsala Dissertations
from the Faculty of Science and Technology 408*

Editor: The Dean of the Faculty of Science and Technology

A doctoral dissertation from the Faculty of Science and Technology, Uppsala University, is usually a summary of a number of papers. A few copies of the complete dissertation are kept at major Swedish research libraries, while the summary alone is distributed internationally through the series Digital Comprehensive Summaries of Uppsala Dissertations from the Faculty of Science and Technology. (Prior to January, 2005, the series was published under the title "Comprehensive Summaries of Uppsala Dissertations from the Faculty of Science and Technology".)



ACTA
UNIVERSITATIS
UPSALIENSIS
UPPSALA
2008

Distribution: publications.uu.se
urn:nbn:se:uu:diva-8574